

**Uncertainty quantification for
spatio-temporal computer models with
calibration-optimal bases**

James M. Salter*

Department of Mathematics, College of Engineering, Mathematics and
Physical Sciences, University of Exeter, UK.

and

Daniel B. Williamson

Department of Mathematics, College of Engineering, Mathematics and
Physical Sciences, University of Exeter, UK.

and

John Scinocca

Canadian Centre for Climate Modelling and Analysis
Victoria, Canada.

and

Viatcheslav Kharin

Canadian Centre for Climate Modelling and Analysis
Victoria, Canada.

June 20, 2022

Abstract

The calibration of complex computer codes using uncertainty quantification (UQ) methods is a rich area of statistical methodological development. When applying these techniques to simulators with spatio-temporal output, it is now standard to use principal component decomposition to reduce the dimensions of the outputs in order to allow Gaussian process emulators to predict the output for calibration. We outline the ‘terminal case’, in which the model cannot reproduce observations to within model discrepancy, and for which standard calibration methods in UQ fail to give sensible results. We show that even when there is no such issue with the model, the standard decomposition on the outputs can and usually does lead to a terminal case analysis. We present a simple test to allow a practitioner to establish whether their experiment will result in a terminal case analysis and a methodology for defining calibration-optimal bases that avoid this whenever it is not inevitable. We apply these ideas to the CanAM4 model to demonstrate the terminal case issue arising for climate models. We discuss climate model tuning and the estimation of model discrepancy within this context, and show how the optimal rotation algorithm can be used in developing practical climate model tuning tools.

1 Introduction

The design and analysis of computer experiments, now known collectively across disciplines as ‘Uncertainty Quantification’ or ‘UQ’, has a rich history

*The authors gratefully acknowledge *support from EPSRC fellowship No. EP/K019112/1 and support from the NSERC funded Canadian Network for Regional Climate and Weather Processes (CNRCWP)*. We would also like to thank *Yanjun Jiao for managing our ensembles of CanAM4*

in statistical methodological development as far back as the landmark paper by Sacks et al. (1989). The calibration of computer simulators, a term reserved for methods that locate simulator input values with outputs that are consistent with physical observations (the inverse problem), is a well studied problem in statistical science, with Kennedy and O’Hagan’s Bayesian approach based on Gaussian processes the most widely used (Kennedy and O’Hagan, 2001).

The essence of the statistical approach to calibration is to combine a formal statistical model relating the computer simulator to real-world processes for which we have partial observations (Kennedy and O’Hagan, 2001; Goldstein and Rougier, 2009; Williamson et al., 2013), with a statistical representation of the relationship between inputs and outputs of the simulator based, typically, on Gaussian processes (Haylock and O’Hagan, 1996).

Extensions for computer simulators with spatio-temporal output have centred around projecting the output onto a basis and adapting calibration methods to the lower-dimensional projections of these fields. Though wavelets (Bayarri et al., 2007) and B-splines (Williamson et al., 2012) have been tried, the approach due to Higdon et al. (2008), based on the principal components of the simulator output, has become the default method. Statistical methodological developments in UQ have built on principal component methods (e.g. Wilkinson (2010); Chang et al. (2014, 2016)), and they have seen wide application, particularly in the analysis of climate models (Sexton et al., 2011; Chang et al., 2014; Pollard et al., 2016).

What statisticians term calibration is referred to as ‘tuning’ in the climate modelling community, a process that has a huge influence on the pro-

jections made by each modelling centre and by the Intergovernmental Panel on Climate Change (Stocker et al., 2013). Each modelling centre submits integrations of their climate model for 4 different forcing scenarios (known as Representative Concentration Pathways) to each phase of the Coupled Model Intercomparison Project (Meehl et al., 2000), with the input parameters of the model ‘tuned’ prior to submission so that the model output compares favourably with certain key observations. The resulting integrations, and not the simulators themselves, are what most climate scientists call “climate models” (i.e. simulators are not considered to be functions of these now fixed parameters). These integrations are used to discover physical mechanisms (Scaife et al., 2012), projected trends (Screen and Williamson, 2017), drivers of variability (Collins et al., 2010) and future uncertainty to aid policy making (Harris et al., 2006).

Despite the application of UQ methods to the calibration of ‘previous-generation’ climate models, referred to in the papers above and many others, UQ is not used for tuning within any of the major climate modelling centres (Hourdin et al., 2017). Instead, climate model parameters are often explored individually and tuning done by hand and eye, with the parameters changed, and the new run either accepted or rejected based on heuristic comparison with the current ‘best’ integration. Different descriptions of these processes are offered by Mauritsen et al. (2012); Williamson et al. (2017); Hourdin et al. (2017).

This lack of uptake of state-of-the-art statistical methodology for calibration amongst some of the world’s most important computer simulators should give us pause for thought. The ‘off-the-shelf’ methodology, Bayesian

calibration with principal components, is widely used elsewhere, well published, and is applied to many lower resolution climate models within the climate science literature. Is the lack of uptake a communication issue or are there features of our methodology that mean it doesn't scale up well to climate simulators?

In this paper we show how the terminal case, wherein a simulator cannot be satisfactorily calibrated, manifests in the inference of standard UQ methodologies. We then demonstrate that even when there is a good solution to the inverse problem, the use of standard basis representations of spatio-temporal output (e.g. principal components across the design) can and regularly do lead to the terminal case and incorrect inference. We develop a simple test to see whether an analysis will lead to the terminal case before performing the calibration and, when the terminal case is not guaranteed, a methodology for finding an optimal basis for calibration. The efficacy of our methodology is demonstrated through application to an idealised example, and its relevance to climate model tuning through application to the calibration of the atmosphere of the current Canadian Climate model CanAM4.

In Section 2 we review UQ methodologies for calibration and present the terminal case for scalar model output. Section 3 reviews the standard approach to handling spatio-temporal output and demonstrates the implications of the terminal case for these methods through an idealised example. We present novel methods for finding optimal bases for calibration that overcome the terminal case issues and demonstrate the efficacy of calibrating with optimal bases for our example. In Section 5 we see that standard

approaches always lead to terminal analyses in CanAM4 and show how our optimal basis methodology can be used to help estimate model discrepancy. Section 6 contains discussion.

2 Calibration methodologies and the terminal case

We consider a computer simulator to be a vector valued function $f(\mathbf{x}, \theta)$, with input parameters \mathbf{x} that we wish to estimate/constrain, and ‘control’ or ‘forcing’ parameters, θ , which can be altered to perform computer experiments. For example, θ might represent future CO₂ concentrations in a climate model. $f(\cdot, \theta)$ simulates a physical system $\mathbf{y}(\theta)$, and we have access to measurements or observations \mathbf{z} of part or all of \mathbf{y} . The goal of calibration methods is to use \mathbf{z} to learn about \mathbf{x} .

The two statistical methodologies for calibration that we focus on here are Bayesian calibration (or probabilistic calibration) (Kennedy and O’Hagan, 2001; Higdon et al., 2008), and history matching with iterative refocussing (Craig et al., 1996; Vernon et al., 2010; Williamson et al., 2017). Both begin with the same type of assumption, namely that there exists a best input setting, \mathbf{x}^* , so that (dropping θ for notational convenience)

$$\mathbf{y} = f(\mathbf{x}^*) + \boldsymbol{\eta}, \quad \mathbf{z} = \mathbf{y} + \mathbf{e} \tag{1}$$

for mean-zero independent observation errors, \mathbf{e} , and model discrepancy, $\boldsymbol{\eta}$ (though history matching differs in only requiring uncorrelated terms in (1) rather than independent terms).

Both methods require an emulator, usually a Gaussian process representation of function $f(\mathbf{x})$, trained using runs $\mathbf{F} = (f(\mathbf{x}_1), \dots, f(\mathbf{x}_n))$ based on design $\mathbf{X} = (\mathbf{x}_1, \dots, \mathbf{x}_n)$. For scalar $f(\cdot)$ the general model is

$$f(\mathbf{x})|\boldsymbol{\beta}, \boldsymbol{\phi} \sim \text{GP}(\boldsymbol{\beta}^T g(\mathbf{x}), R(|\mathbf{x} - \mathbf{x}'|; \boldsymbol{\phi})), \quad (2)$$

where $g(\mathbf{x})$ is a vector of specified regressors, $\boldsymbol{\beta}$ their coefficients, and $R(|\mathbf{x} - \mathbf{x}'|; \boldsymbol{\phi})$ a weakly stationary covariance function with parameters $\boldsymbol{\phi}$. The model is completed by specifying a prior on the parameters $\pi(\boldsymbol{\beta}, \boldsymbol{\phi})$, and posterior inference given \mathbf{F} follows naturally with

$$f(\mathbf{x})|\mathbf{F}, \boldsymbol{\beta}, \boldsymbol{\phi} \sim \text{GP}(m^*(\mathbf{x}), R^*(\cdot, \cdot; \boldsymbol{\phi}))$$

with

$$m^*(\mathbf{x}) = \boldsymbol{\beta}^T g(\mathbf{x}) + \mathbf{K}(\mathbf{x})\mathbf{V}^{-1}(\mathbf{F} - \boldsymbol{\beta}^T g(\mathbf{X})), \quad R^*(\mathbf{x}, \mathbf{x}'; \boldsymbol{\phi}) = R(\mathbf{x}, \mathbf{x}'; \boldsymbol{\phi}) - \mathbf{K}(\mathbf{x})\mathbf{V}^{-1}\mathbf{K}(\mathbf{x}')^T$$

$$\mathbf{K}(\mathbf{x}) = R(\mathbf{x}, \mathbf{X}, \boldsymbol{\phi}), \quad \mathbf{V} = R(\mathbf{X}, \mathbf{X}, \boldsymbol{\phi}).$$

There are many variants on emulation, with some practitioners preferring no regressors (Chen et al., 2016), different types of correlation function (including no correlation) (Kaufman et al., 2011; Salter and Williamson, 2016), and different priors $\pi(\boldsymbol{\beta}, \boldsymbol{\phi})$ with some leading to partially analytic posterior inference (Haylock and O’Hagan, 1996). As history matching only requires posterior means and variances of the emulator, Bayes linear analogues are sometimes used (Vernon et al., 2010). Generalisations to multivariate Gaussian processes are natural (Conti and O’Hagan, 2010), and we address the

difficulty with high dimensional output from Section 3 onwards.

2.1 Probabilistic calibration

Though the underlying statistical model and the emulator are similar for both history matching and probabilistic calibration, the assumptions placed upon \mathbf{x}^* and the resulting inference are quite different. Probabilistic calibration places a prior on \mathbf{x}^* , $\pi(\mathbf{x}^*)$, and gives a variance for a Gaussian process representation for the discrepancy, $\boldsymbol{\eta} \sim \text{GP}(0, \boldsymbol{\Sigma}_{\boldsymbol{\eta}})$, so that calibration involves observing the marginal posterior $\pi(\mathbf{x}^*, \boldsymbol{\eta} | \mathbf{F}, \mathbf{z})$ for \mathbf{x}^* . The discussion of Kennedy and O’Hagan (2001) and the later paper by Brynjarsdóttir and O’Hagan (2014) argue that lack of identifiability between \mathbf{x}^* and $\boldsymbol{\eta}$ mean that strong prior information on $\boldsymbol{\eta}$ is essential for effective probabilistic calibration to be possible. We hence do not consider the case where an uninformative prior is placed on $\boldsymbol{\Sigma}_{\boldsymbol{\eta}}$ and the discrepancy variance and best inputs jointly inferred in this paper.

2.2 History matching and iterative refocussing

Note that, given a discrepancy variance, probabilistic calibration must still give a posterior $\pi(\mathbf{x}^* | \mathbf{F}, \mathbf{z})$ that integrates to 1, thus predetermining an analysis that will point to some region of parameter space χ as being ‘most likely’. This is undesirable in some application areas, as often the goal is to find out if the simulator *can* get ‘close enough’ to the observations so that computer experiments predicting the future can be trusted. Climate model tuning is a good example of this, where part of the goal in tuning is to find out whether it is the choice of parameters or the parameterisation itself that is leading

model bias (Mauritsen et al., 2012; Hourdin et al., 2017).

The method of history matching and iterative refocussing allows the question of whether the model is fit for purpose to be answered as part of the calibration exercise, by altering the problem from one of looking for the best input directly, to one of trying to rule out regions of χ that could not contain \mathbf{x}^* . A model unfit for purpose would have all of χ ruled out. The method defines an implausibility measure, $\mathcal{I}(\mathbf{x})$, with

$$\mathcal{I}(\mathbf{x}) = (\mathbf{z} - \mathbb{E}[f(\mathbf{x})])^T (\text{Var}(\mathbf{z} - \mathbb{E}[f(\mathbf{x})]))^{-1} (\mathbf{z} - \mathbb{E}[f(\mathbf{x})]). \quad (3)$$

If $\mathcal{I}(\mathbf{x})$ exceeds a threshold, T , that value of \mathbf{x} is considered implausible and ruled out, thus defining a membership function for a subspace of χ that is Not Ruled Out Yet (NROY). A key principle behind the approach is its iterative nature. Following an initial set of runs, a ‘wave’ of history matching is conducted, leading to a certain percentage of χ being ruled out. A new wave can then be designed within NROY space, and the procedure repeated, refocussing the search for possible \mathbf{x}^* (Vernon et al., 2010; Williamson et al., 2017).

The choice of T will be problem dependent, though typically, if \mathbf{z} is one-dimensional, Pukelsheim’s three sigma rule (Pukelsheim, 1994) is used to set $T = 9$ (Craig et al., 1996; Williamson et al., 2015). For l -dimensional \mathbf{z} , Vernon et al. (2010) define $T = \chi_{l,0.995}^2$, the 99.5th percentile of the χ^2 -distribution with l degrees of freedom.

Discrepancy and observation error variances, Σ_{η} and $\Sigma_{\mathbf{e}}$, are important in both probabilistic calibration and history matching. For the latter,

equation (1) leads to

$$\text{Var}(\mathbf{z} - \mathbb{E}[f(\mathbf{x})]) = \text{Var}[f(\mathbf{x})] + \boldsymbol{\Sigma}_\eta + \boldsymbol{\Sigma}_e,$$

whilst a Normal assumption on \mathbf{e} in calibration means $\boldsymbol{\Sigma}_\eta$ and $\boldsymbol{\Sigma}_e$ appear in the likelihood.

In this paper, we focus on optimal spatio-temporal calibration for both types of methodology, as the issues we shall identify in Section 3 apply equally to both, though manifest in different ways as we shall illustrate now with our discussion of the terminal case.

2.3 The terminal case

Consider a computer simulator, $f(\mathbf{x})$, and a discrepancy variance assessment $\boldsymbol{\Sigma}_\eta$ and observation error variance $\boldsymbol{\Sigma}_e$ so that \mathbf{z} , under equation (1), is not consistent with our simulator for an $\mathbf{x} \in \chi$. Within the history matching framework, the interpretation of $\boldsymbol{\Sigma}_\eta$ is of a tolerance of the modellers to model error, so that this situation, the ‘terminal case’, implies that without introducing an emulator, $\mathcal{I}(\mathbf{x}) > T$ for all \mathbf{x} . Hence, all of χ is ruled out and the modellers must reconsider their simulator, or their error tolerance.

Within a probabilistic calibration framework, the terminal case implies a prior-data conflict so that, in some sense, $\boldsymbol{\Sigma}_\eta$ has been ‘misspecified’ or the expert is ‘wrong’. Given the need for informative expert judgement for $\boldsymbol{\Sigma}_\eta$ (Brynjarsdóttir and O’Hagan, 2014), and the difficulty in providing such judgements for complex computer simulators (Goldstein and Rougier, 2009), this may be a common situation so it is important to see how such

prior-data conflict would manifest.

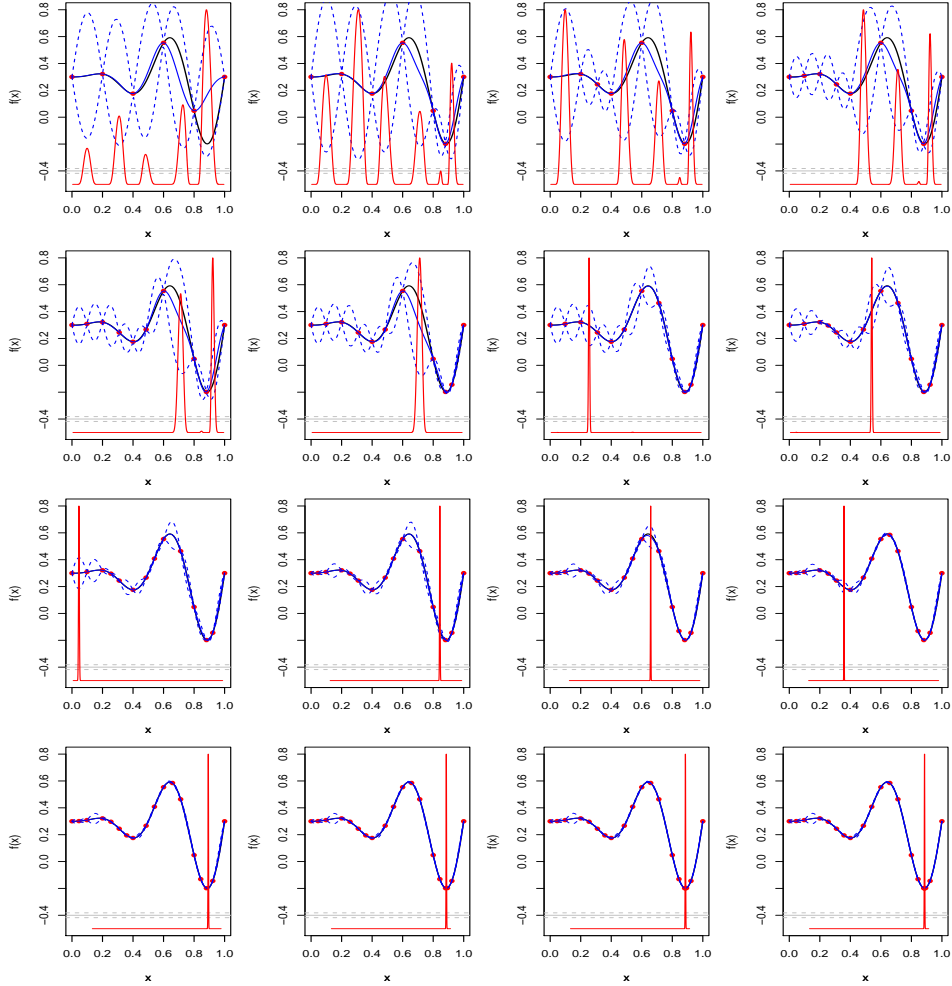


Figure 1: Showing 20 steps of an iterative probabilistic calibration of a computer simulator (black line) to observations (solid grey line) with Σ_{η} and Σ_{ϵ} misspecified (dashed grey lines ± 3 standard deviations). Observations of the model (red dots) iteratively taken at the MAP estimate for \mathbf{x}^* following the fitting of a GP emulator (mean solid blue line, ± 2 standard deviations dashed blue lines), and the posterior distribution of \mathbf{x}^* overlaid at each step (solid red line).

Figure 1 shows 20 steps of an iterative probabilistic calibration of a 1d

$f(\mathbf{x})$ that we can evaluate quickly (black line), to observations (solid grey line) with $\Sigma_{\boldsymbol{\eta}}$ and $\Sigma_{\mathbf{z}}$ misspecified (dashed grey lines ± 3 standard deviations) so that the true function does not come as close to the observations as the expert judgement indicates. Starting with an equally spaced 6 point design, a Gaussian process emulator is fitted for fixed correlation length (mean function is solid blue line, 2 standard deviation intervals given by the blue dashed lines), and the posterior distribution $\pi(\mathbf{x}^* | \mathbf{z}, \mathbf{F})$ overlaid (solid red line). We then evaluate $f(\mathbf{x})$ at the maximum a posteriori estimate for \mathbf{x}^* , refit our Gaussian process and compute the new posterior over \mathbf{x}^* to produce the next plot.

From panel 6 onwards we see the issue with the terminal case for probabilistic calibration. Our posterior beliefs are highly peaked at one particular \mathbf{x} value, yet evaluating the model there completely shifts the peak to a location for which we had near zero prior density. Each evaluation of the simulator, which for climate models may take weeks or months, shifts the posterior spike to an unexpected (a priori) part of parameter space. It is often not efficient to run expensive simulators such as climate models that require expert time to run and manage one run at a time (Williamson, 2015). The scientists that manage jobs on supercomputers, for example, require batches of runs that can be run in parallel. However, batch designs would be even worse here. Guided by the posterior density at each point, batch designs would be the near equivalent of one point at the MAP estimate, simply shifting the peak of the posterior to somewhere as yet unsampled.

Eventually, as we see from the bottom 4 panels, posterior uncertainty in $f(\mathbf{x})$ is sufficiently reduced and $\pi(\mathbf{x}^* | \mathbf{F}, \mathbf{z})$ settles on the ‘least bad’

value of \mathbf{x} , where $f(\mathbf{x})$ is closest to the observations (though around 30 standard deviations away). For simulators with input spaces of much higher dimensions (the climate models we work with have typically specified 10-30 parameters to focus on, though these would be a subset of several hundred), we are unlikely to ever be able to reduce emulator uncertainty to the extent that the posterior spike settles over the least bad parameter setting. Hence, under an iterative procedure such as this, we would continue to chase the best input throughout parameter space, constantly moving the spike as in a game of whack-a-mole, until we run out of resources.

Arguably, if in the terminal case, history matching is the preferred methodology (a case argued by, for example, Williamson et al. (2013)). In the example, all of χ is ruled out after 2 iterations. However, given a stopping rule, the same inference could be drawn by extending the probabilistic calibration methodology. We can also combine methods, by first history matching to check that the terminal case does not apply, before performing a probabilistic calibration within NROY space, as in Salter and Williamson (2016). Whichever calibration method, or combination of them, is preferred, it is important to understand this terminal case, as we shall see that even for models that can reproduce observations exactly, tractable methods for calibrating high dimensional output can result in a terminal case analysis.

3 Calibration with spatio-temporal output

For spatio-temporal fields, the most common approach to emulation and calibration involves projecting the model output onto a low-dimensional

basis $\mathbf{\Gamma}$ and emulating the coefficients, so that fewer emulators are required (Bayarri et al., 2007; Higdon et al., 2008; Wilkinson, 2010; Sexton et al., 2011) (although alternatives, such as emulating every grid box individually, have been applied, e.g. by Gu et al. (2016)).

Writing the model output $f(\mathbf{x}_i)$ as a vector of length l , so that \mathbf{F} has dimension $l \times n$, the singular value decomposition (SVD) is used to give n eigenvectors that can be used as basis vectors (equivalently, finding the principal components or EOFs) (Higdon et al., 2008; Wilkinson, 2010; Sexton et al., 2011; Chang et al., 2014, 2016). For the size of model output typically explored using these methods, \mathbf{F} will not be of full rank as $n \ll l$. This means that while \mathbf{F} can be represented exactly by projection onto $\mathbf{\Gamma}$, general l -dimensional fields will not have a perfect representation on $\mathbf{\Gamma}$. As the majority of the variability in \mathbf{F} is usually explained by only the first few eigenvectors, the basis is truncated after q vectors, giving a basis $\mathbf{\Gamma}_q = (\gamma_1, \dots, \gamma_q)$ of dimension $l \times q$, often chosen so that more than 95% of \mathbf{F} is explained by $\mathbf{\Gamma}_q$. Various rules-of-thumb are used dependent on the problem, e.g. Higdon et al. (2008) truncate after 99%, while Chang et al. (2014) use 90%.

In order to emulate the model, we first centre the runs by subtracting their mean, $\boldsymbol{\mu}$, from each column of \mathbf{F} , giving the centred ensemble \mathbf{F}_μ (we use the term ensemble to mean the collection of runs, as is common in the study of climate models). We then project \mathbf{F}_μ onto the basis $\mathbf{\Gamma}_q$, giving q coefficients associated with each parameter choice:

$$\mathbf{c}(\mathbf{x}_i) = (\mathbf{\Gamma}_q^T \mathbf{\Gamma}_q)^{-1} \mathbf{\Gamma}_q^T (f(\mathbf{x}_i) - \boldsymbol{\mu}) \quad (4)$$

Given q coefficients, we can reconstruct a field of size l via

$$f(\mathbf{x}_i) = \mathbf{\Gamma}_q \mathbf{c}(\mathbf{x}_i) + \boldsymbol{\mu} + \boldsymbol{\epsilon}, \quad (5)$$

with $\boldsymbol{\epsilon} = \mathbf{0}$ for $\mathbf{x}_i \in \mathbf{X}$.

We build emulators for the coefficients of the first q SVD basis vectors:

$$c_i(\mathbf{x}) \sim \text{GP}(m_i^*(\mathbf{x}), R_i^*(\mathbf{x}, \mathbf{x}; \boldsymbol{\phi})), \quad i = 1, \dots, q. \quad (6)$$

Given these emulators, calibration can either be performed using the entire l -dimensional output, with emulator expectations and variances transformed to the l -dimensional space of the original field (Wilkinson, 2010), or on its q -dimensional basis representation, with the observations projected onto this basis (Higdon et al., 2008).

When using a basis emulator to calibrate $f(\cdot)$, we may incorrectly conclude that we are in the terminal case as reconstructions from coefficients on the basis are restricted to a q -dimensional subspace of l -dimensional space. Further, it will not be clear whether this implies that the model is incapable of reproducing \mathbf{z} , or that this was due to a poor basis choice. The SVD basis chooses this q -dimensional subspace to explain the maximum amount of variability in \mathbf{F} with the fewest number of basis vectors. This does not guarantee that important directions in \mathbf{F} that are consistent with \mathbf{z} are preserved.

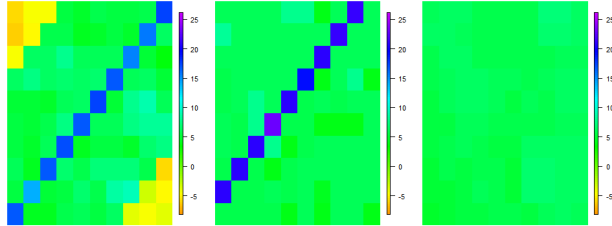


Figure 2: Left: the observations, \mathbf{z} , for our function. Centre: the ensemble mean. Right: the reconstruction of \mathbf{z} using the truncated SVD basis.

3.1 Illustrative example

We illustrate this problem with an idealised example of a 6 parameter function $f(\mathbf{x})$ (detailed in Section S1), with output given over a 10×10 grid. Observations, \mathbf{z} , are given by a known input parameter setting, $f(\mathbf{x}^*)$, with $N(0, \Sigma_e)$ observation error added (given in (S2)), so that a calibration exercise should be able to identify \mathbf{x}^* . In our example the great majority of the input space leads to output that is biased away from \mathbf{z} , so that the proportion of input space leading to output consistent with \mathbf{z} is around 0.01% of χ .

The first panel of Figure 2 shows the observations, \mathbf{z} , with a strong signal on the main diagonal. The second panel is the mean of the output field over a maximin Latin hypercube sample of size 60 in χ . We refer to this sample as an ensemble, \mathbf{F} . The strong signal in the ensemble is a biased version of \mathbf{z} . In a climate context, this is analogous to the Gulf Stream being observed in the incorrect place in model output.

We subtract the ensemble mean (Figure 2, centre panel) from each run in \mathbf{F} and calculate the SVD of the centred ensemble \mathbf{F}_μ , giving the SVD basis

$\mathbf{\Gamma}$ (these are the right singular vectors of \mathbf{F}_μ). Over 95% of the ensemble variability is explained by projection onto the first four basis vectors, which we refer to as $\mathbf{\Gamma}_4$, or the ‘truncated basis’. However, if we project \mathbf{z} onto this basis, and reconstruct the original field using these coefficients via equations (4) and (5), we have the field given by the third panel of Figure 2: the distinctive pattern found in \mathbf{z} has been lost. This reconstruction is made with the true coefficients for \mathbf{z} , hence regardless of how accurate we can emulate these coefficients, we cannot find fields that are consistent with \mathbf{z} using this basis, as this reconstruction is the ‘best’ representation of \mathbf{z} allowed by $\mathbf{\Gamma}_4$. The same happens for any realisation from $N(f(\mathbf{x}^*), \mathbf{\Sigma}_e)$, establishing that, for reconstructions of the field using $\mathbf{\Gamma}_4$, we are in the terminal case.

Fitting Gaussian process emulators to the coefficients given by projection of \mathbf{F}_μ onto the four basis vectors, the expectation and variance at \mathbf{x} is given by

$$\begin{aligned} \mathbb{E}[\mathbf{c}(\mathbf{x})] &= (\mathbb{E}[c_1(\mathbf{x})], \dots, \mathbb{E}[c_4(\mathbf{x})])^T, \\ \text{Var}[\mathbf{c}(\mathbf{x})] &= \text{diag}(\text{Var}[c_1(\mathbf{x})], \dots, \text{Var}[c_4(\mathbf{x})]). \end{aligned}$$

To probabilistically calibrate or history match on the original field, we require $\mathbb{E}[f(\mathbf{x})]$ and $\text{Var}[f(\mathbf{x})]$ in terms of the coefficient emulators. These are

$$\begin{aligned} \mathbb{E}[f(\mathbf{x})] &= \mathbf{\Gamma}_q \mathbb{E}[\mathbf{c}(\mathbf{x})] \\ \text{Var}[f(\mathbf{x})] &= \mathbf{\Gamma}_q \text{Var}[\mathbf{c}(\mathbf{x})] \mathbf{\Gamma}_q^T + \mathbf{\Gamma}_{-q} \mathbf{\Sigma}_{-q} \mathbf{\Gamma}_{-q}^T \end{aligned}$$

where $\mathbf{\Gamma}_{-q}$ contains the discarded basis vectors, and $\mathbf{\Sigma}_{-q}$ is a diagonal matrix with the associated eigenvalues as the diagonal elements (Wilkinson, 2010).

Calibrating in the coefficient subspace requires projection of \mathbf{z} , $\mathbf{\Sigma}_\eta$ and $\mathbf{\Sigma}_e$ onto $\mathbf{\Gamma}_4$. For example, the implausibility in (3) on the coefficients becomes

$$\mathcal{I}_c(\mathbf{x}) = (\mathbf{\Gamma}_q^T \mathbf{z} - \mathbb{E}[\mathbf{c}(\mathbf{x})])^T (\text{Var}[\mathbf{c}(\mathbf{x})] + \mathbf{\Gamma}_q^T \mathbf{\Sigma}_\eta \mathbf{\Gamma}_q + \mathbf{\Gamma}_q^T \mathbf{\Sigma}_e \mathbf{\Gamma}_q)^{-1} (\mathbf{\Gamma}_q^T \mathbf{z} - \mathbb{E}[\mathbf{c}(\mathbf{x})]). \quad (7)$$

For the example, as established above, we are in the terminal case, so probabilistic calibration on the field gives peaked prediction at the incorrect value of \mathbf{x}^* consistent with the description given in section 2.3 (see SM section S1.1, Figures S3, S4).

Using the 0.995 value of the chi-squared distribution with 100 degrees of freedom to history match via (3), we rule out the whole parameter space, χ . By history matching on the coefficients instead using (7), ruling out runs based on the chi-squared distribution with 4 degrees of freedom, we find an NROY space consisting of 3.8% of χ . However, we can check whether we are accurately ruling out space, by evaluating our function at each \mathbf{x} and history matching without the presence of emulation. Doing so, we find that we have ruled out 58% of runs that are in fact consistent with \mathbf{z} using the SVD basis.

Whether we are calibrating on the original field, or on the coefficients, the ‘best’ result we are able to find is that given by the reconstruction of \mathbf{z} with $\mathbf{\Gamma}_4$ given in the final panel of Figure 2. On the field, we are in the terminal case. On the coefficients, we are attempting to find runs that give coefficients

that lead to this reconstruction, regardless of what happens in the directions we are interested in (i.e. the main diagonal pattern). Furthermore, if we are able to run a new ensemble on an expensive model, based on calibration results, we are less likely to do so if our predictive fields appear inconsistent with \mathbf{z} , as guaranteed by this basis. Henceforth, we choose to focus on calibration on the field, as it compares all aspects of the observed output to the model, rather than a few summaries of it.

4 Optimal basis selection

There are two main requirements for the basis representation of high-dimensional output: being able to represent \mathbf{z} with the basis (a feature not guaranteed by principal component methods), and retaining enough signal in the chosen subspace to enable accurate emulators to be built for the basis coefficients (as principal components do). A natural method for satisfying the first goal is to minimise the error given when the observations are reconstructed using the basis. The second is harder to quantify. Here, the proportion of variability explained by projection of the ensemble onto each basis vector is used: as this decreases, there is less signal given by projection onto a basis vector, and it may become more difficult to build an accurate emulator for the coefficients.

The proportion of ensemble variability explained by a basis \mathbf{B} can be written as

$$\mathcal{V}(\mathbf{B}, \mathbf{F}) = \frac{\sum_{i=1}^l \sum_{j=1}^n [\mathbf{B}(\mathbf{B}^T \mathbf{B})^{-1} \mathbf{B}^T \mathbf{F}]_{ij}^2}{\sum_{i=1}^l \sum_{j=1}^n \mathbf{F}_{ij}^2} \quad (8)$$

We similarly define the variance explained by projection onto a single basis

vector \mathbf{b}_k as

$$\mathcal{V}_k(\mathbf{B}, \mathbf{F}) = \frac{\sum_{i=1}^l \sum_{j=1}^n [\mathbf{b}_k(\mathbf{b}_k^T \mathbf{b}_k)^{-1} \mathbf{b}_k^T \mathbf{F}]_{ij}^2}{\sum_{i=1}^l \sum_{j=1}^n \mathbf{F}_{ij}^2} \quad (9)$$

The SVD basis maximises $\mathcal{V}_k(\mathbf{B}, \mathbf{F})$ for each k , given the previous vectors. However, when the observations are not consistent with the ensemble, aiming to explain as much variability as possible with as few basis vectors, as in SVD, is not a suitable approach.

4.1 Reconstruction error

We quantify the difference between the observations, \mathbf{z} , and its reconstruction using a given basis \mathbf{B} , by defining the ‘reconstruction error’:

$$\mathcal{R}_{\mathbf{W}}(\mathbf{B}, \mathbf{z}) = \|\mathbf{z} - \mathbf{B}(\mathbf{B}^T \mathbf{B})^{-1} \mathbf{B}^T \mathbf{z}\|_{\mathbf{W}} \quad (10)$$

where

$$\|\mathbf{z} - \mathbf{r}(\mathbf{z})\|_{\mathbf{W}} = (\mathbf{z} - \mathbf{r}(\mathbf{z}))^T \mathbf{W}^{-1} (\mathbf{z} - \mathbf{r}(\mathbf{z})) \quad (11)$$

and \mathbf{W} is an $l \times l$ positive-definite weight matrix. By setting $\mathbf{W} = \boldsymbol{\Sigma}_{\mathbf{e}} + \boldsymbol{\Sigma}_{\boldsymbol{\eta}}$, this is analogous to (3), and is the implausibility when we know the basis coefficients exactly (so that the emulator variance is 0).

Prior to building emulators and performing calibration for a given basis, we can assess whether we expect to be able to find fields similar to \mathbf{z} , given the observation error and discrepancy variances. For history matching threshold T , if

$$\mathcal{R}_{\mathbf{W}}(\mathbf{B}, \mathbf{z}) > T \quad (12)$$

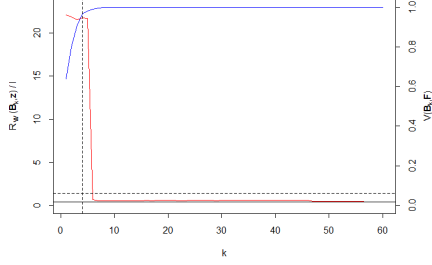


Figure 3: A plot showing how the reconstruction error (red) and percentage of ensemble variability explained (blue) change as the SVD basis is increased in size, for $\mathbf{W} = \Sigma_{\mathbf{e}} + \Sigma_{\boldsymbol{\eta}}$.

then we will rule out the representation of \mathbf{z} on this basis, even if we can perfectly emulate the coefficients. We see then that (12) provides a test to see whether a given basis will lead to a terminal case analysis, whether or not reasonable values of \mathbf{x}^* exist. If (12) holds for some $\{\mathbf{B}, \mathbf{W}\}$, we may view \mathbf{W} as having been misspecified, i.e. we have not accounted for the correct amount of model discrepancy. However, we may also have under-explored the output dimension of $f(\cdot)$ so that \mathbf{B} does not allow us to get close enough to \mathbf{z} . We revisit this test in the context of optimal basis choice in section 4.3.

Figure 3 compares $\mathcal{V}(\cdot, \mathbf{F}_{\boldsymbol{\mu}})$ and $\mathcal{R}_{\mathbf{W}}(\cdot, \mathbf{z})$ for the example of Section 3. We refer to plots of this type as VarMSE plots. The red line represents $\mathcal{R}_{\mathbf{W}}(\mathbf{B}_k, \mathbf{z})$, and the blue line shows $\mathcal{V}(\mathbf{B}_k, \mathbf{F}_{\boldsymbol{\mu}})$, for each truncated basis, $\{\mathbf{B}_k\}_{k=1}^n$. The vertical dotted line indicates where the basis is truncated if we wish to explain 95% of the ensemble variability, and the horizontal dotted line represents the history matching bound, T . The solid horizontal line is equal to $\mathcal{R}_{\mathbf{W}}(\mathbf{B}, \mathbf{z})$. For the SVD basis in our example, we see that $\mathcal{R}_{\mathbf{W}}(\cdot, \mathbf{z})$ is large (compared to T) until $k = 6$, where the error decreases below the

threshold, indicating that the sixth basis vector contains patterns that are important for explaining \mathbf{z} . As further basis vectors are added, $\mathcal{R}_{\mathbf{W}}(\cdot, \mathbf{z})$ continues to decrease, suggesting that patterns relevant for representing \mathbf{z} are in fact included in $\mathbf{\Gamma}$ for this example. However, as the later basis vectors explain low percentages of the variability in the ensemble, accurate emulation is not possible here.

The SVD basis aims to maximise the blue line for each basis vector added, whereas, for calibration, we require the red line to be below T . The problem of basis selection for calibration is one of trading off these two requirements, reducing $\mathcal{R}_{\mathbf{W}}(\cdot, \mathbf{z})$ while ensuring that each $\mathcal{V}_k(\cdot, \mathbf{F}_{\boldsymbol{\mu}})$ is large enough to enable emulators to be built. Given that the full SVD basis may contain information and patterns that allow the observations to be more accurately represented, the information contained in this basis may be combined in such a way that the resulting basis is suitable for calibration, with important low-order patterns blended with those that explain more of the ensemble variability.

4.2 Rotating a basis

Performing a rotation of the SVD basis $\mathbf{\Gamma}$ using an $n \times n$ rotation matrix $\mathbf{\Lambda}$ rearranges the signal from the ensemble, potentially allowing the new truncated basis to be a better representation of \mathbf{z} . A general $n \times n$ rotation matrix $\mathbf{\Lambda}$ can be defined by composing $n(n-1)/2$ matrices that give a rotation by an angle around each pair of dimensions (Murnaghan, 1962). Our goal is to find $\mathbf{\Lambda}$ such that $\mathbf{\Gamma}\mathbf{\Lambda}$ minimises $\mathcal{R}_{\mathbf{W}}((\mathbf{\Gamma}\mathbf{\Lambda})_q, \mathbf{z})$, subject to constraints on $\mathcal{V}_k(\cdot, \mathbf{F}_{\boldsymbol{\mu}})$ that allow each rotated basis coefficient to be emulated.

To directly define a rotation matrix $\mathbf{\Lambda}$ via optimisation requires a large number of angles to be found, even when the ensemble size is small. Instead we take an iterative approach, selecting new basis vectors sequentially while minimising $\mathcal{R}_{\mathbf{W}}(\cdot, \mathbf{z})$ at each step in such a way that guarantees that the resulting basis is an orthogonal rotation of the original basis.

Given $p < n$ basis vectors, $\mathbf{B}_p = (\mathbf{b}_1, \dots, \mathbf{b}_p)$, we define the ‘ensemble residual’ as

$$\mathbf{F}_\epsilon = \mathbf{F}_\mu - \mathbf{B}_p(\mathbf{B}_p^T \mathbf{B}_p)^{-1} \mathbf{B}_p^T \mathbf{F}_\mu$$

This represents the variability in the ensemble not explained by \mathbf{B}_p . Define the ‘residual basis’, \mathbf{B}_ϵ , to be the matrix containing the right singular vectors of \mathbf{F}_ϵ . The residual basis gives us basis vectors that explain the remaining variability in \mathbf{F}_μ , given vectors \mathbf{B}_p .

4.3 The optimal rotation algorithm

Given an orthogonal basis \mathbf{B} for \mathbf{F}_μ with dimension $l \times n$, a positive definite $l \times l$ weight matrix \mathbf{W} , a vector \mathbf{v} containing values for the minimum proportion of the ensemble variability to be explained by a single basis vector, the total proportion of ensemble variability to be explained by the basis v_{tot} , and a bound T (usually that implied by history matching, $T = \chi_{0.995, l}^2$), we find an optimal basis for performing calibration as follows:

1. If $\mathcal{R}_{\mathbf{W}}(\mathbf{B}, \mathbf{z}) > T$, stop and revisit the specification of \mathbf{W} . Else set $k = 1$.

2. Let $\mathbf{\Gamma}_k^* = (\gamma_1^*, \dots, \gamma_{k-1}^*, \mathbf{B}\boldsymbol{\lambda}_k)$ and set

$$\boldsymbol{\lambda}_k^* = \operatorname{argmin}_{\boldsymbol{\lambda}_k} \|\mathbf{z} - \mathbf{\Gamma}_k^* (\mathbf{\Gamma}_k^{*T} \mathbf{\Gamma}_k^*)^{-1} \mathbf{\Gamma}_k^{*T} \mathbf{z}\|_{\mathbf{W}}$$

such that $\mathcal{V}_k(\mathbf{\Gamma}_k^*, \mathbf{F}\boldsymbol{\mu}) \geq v_k$. Define the new normalised vector as

$$\gamma_k^* = \frac{\mathbf{B}\boldsymbol{\lambda}_k^*}{\|\mathbf{B}\boldsymbol{\lambda}_k^*\|}$$

and set $\mathbf{\Gamma}_k^* = (\gamma_1^*, \dots, \gamma_{k-1}^*, \gamma_k^*)$.

3. Find the residual basis given $\mathbf{\Gamma}_k^*$, \mathbf{B}_ϵ , and form the orthogonal rank n basis

$$\mathbf{\Gamma}^* = (\mathbf{\Gamma}_k^*, [\mathbf{B}_\epsilon]_{n-k})$$

4. Define $q \geq k$ as the minimum value satisfying $\mathcal{V}(\mathbf{\Gamma}_q^*, \mathbf{F}\boldsymbol{\mu}) \geq v_{tot}$, where $\mathbf{\Gamma}_q^*$ represents the first q columns of $\mathbf{\Gamma}^*$. If $\mathcal{R}_{\mathbf{W}}(\mathbf{\Gamma}_q^*, \mathbf{z}) < T$, then stop, and return $\mathbf{\Gamma}_q^*$ as the truncated basis for calibration. Else, set $k = k+1$ and $\mathbf{B} = \mathbf{B}_\epsilon$, and return to step 2.

Our algorithm selects the linear combination of a given basis, at each step, that minimises $\mathcal{R}_{\mathbf{W}}(\cdot, \mathbf{z})$, given any previously selected basis vectors. If the truncation $\mathbf{\Gamma}_q^*$ satisfies $\mathcal{R}_{\mathbf{W}}(\mathbf{\Gamma}_q^*, \mathbf{z}) < T$, then the algorithm terminates, as standard residual variance maximising basis vectors no longer lead to a terminal case analysis. We allow a basis to be identified that satisfies our two goals: we do not rule out \mathbf{z} , and have coefficients that can be emulated, if \mathbf{v} is set appropriately.

The check in step 1 of our algorithm is due to the following result (proved

in S2):

Result 1 (Invariance of $\mathcal{R}_{\mathbf{W}}(\cdot, \cdot)$ to rotation). *For a rotation matrix $\mathbf{\Lambda}$ of dimension $k \times k$, and a set of basis vectors $\mathbf{B} = (\mathbf{b}_1, \dots, \mathbf{b}_n)$, we have*

$$\mathcal{R}_{\mathbf{W}}(\mathbf{B}_k, \mathbf{z}) = \mathcal{R}_{\mathbf{W}}(\mathbf{B}_k \mathbf{\Lambda}, \mathbf{z}), \quad k = 1, \dots, n \quad (13)$$

Regardless of the rotation that is applied to $\mathbf{\Gamma}$, we cannot reduce the reconstruction error below that given by the full basis originally. However, because the SVD basis is always truncated prior to this minimum value being reached, we can find a rotation that rearranges the information from the SVD basis in such a way that we have

$$\mathcal{R}_{\mathbf{W}}((\mathbf{B}\mathbf{\Lambda})_q, \mathbf{z}) \ll \mathcal{R}_{\mathbf{W}}(\mathbf{B}_q, \mathbf{z}) \quad (14)$$

incorporating important, potentially low-order, patterns into the q basis vectors that we emulate. Hence step 1 of the algorithm provides an important test as to whether our ensemble and uncertainty assessment (\mathbf{F}, \mathbf{W}) are sufficient to avoid a terminal case analysis.

Theorem 1. $\mathbf{\Gamma}^*$ *in step 3 of the optimal rotation algorithm is an orthogonal rotation of \mathbf{B} .*

The results and proofs required, and the proof of the theorem itself, are found in Section S2. Hence, given an orthonormal basis, \mathbf{B} , for \mathbf{F}_{μ} , the optimal rotation algorithm finds a rotation and truncation that avoids a terminal case analysis (if such a rotation exists), whilst ensuring the emulatability of the coefficients of the resulting projection.

In an application, it may be desirable to include certain physical patterns that are deemed to be important in our basis \mathbf{B} , which may not lie within the subspace defined by \mathbf{F}_μ . In this case, if we have p selected physical vectors, $\mathbf{B}_p = (\mathbf{b}_1, \dots, \mathbf{b}_p)$, combining these with the first $n - p$ vectors of the residual basis will not necessarily explain all of the variability in \mathbf{F}_μ . The algorithm may be applied to the $n + p$ vectors given by the physical vectors and the full residual basis, giving a rotation of this space rather than of \mathbf{F}_μ . As truncation occurs after the majority of variability of \mathbf{F}_μ , v_{tot} , is explained, the resulting truncated basis, while not strictly a rotation of the subspace defined by \mathbf{F}_μ , will exhibit similar qualities, and may be superior for representing \mathbf{z} , if important physical patterns can be emulated when combined with signal from the ensemble.

To perform the algorithm with basis vectors from outside the subspace defined by \mathbf{F}_μ , rather than finding linear combinations of the residual basis at step $k > 1$, $\mathbf{B} = (\mathbf{B}_p, \mathbf{B}_\epsilon)$ is used at each step, with orthogonality imposed after each new basis vector has been selected, via Gram-Schmidt (as by Result S3, applying Gram-Schmidt does not affect $\mathcal{R}_\mathbf{W}(\cdot, \mathbf{z})$).

Prior to applying the algorithm, we must specify an initial basis, \mathbf{B} , a weight matrix, \mathbf{W} , and the parameters v_{tot} and \mathbf{v} to control the amount of variability explained by each basis vector. We use the SVD basis for \mathbf{B} as its computation is efficient, however other choices are possible. For \mathbf{W} , a natural choice is $\mathbf{W} = \mathbf{\Sigma}_\epsilon + \mathbf{\Sigma}_\eta$, due to the parallel between $\mathcal{R}_\mathbf{W}(\cdot, \mathbf{z})$ and the implausibility (3), so that the check for the terminal case is informative.

Constraints must be set for $\mathcal{V}_k(\cdot, \mathbf{F}_\mu)$ via a vector \mathbf{v} that contains the minimum proportion of \mathbf{F}_μ that must be explained by the k^{th} new basis

vector. In practice, when applying our algorithm to high dimensional model output, we have found that only a small number (three or fewer) of iterations have been required, hence \mathbf{v} often has a low dimension. The values of \mathbf{v} are highly dependent on the problem, with a different approach required when a small number of vectors explain the majority of the ensemble, compared to when a large proportion of the variability is spread across many SVD basis vectors. In the former case, the values of \mathbf{v} may be relatively high, whilst in the latter they can be lower, relative to the proportion explained by the equivalent SVD basis vectors.

Similarly, the total proportion of variability that the rotated basis must explain, v_{tot} , is problem dependent. When the variability is spread across a large number of vectors, this should be given a smaller value than if only a small number are needed to explain 95% or 99% in the SVD basis. We note that this last issue is also a concern for the standard UQ approaches based on principal components.

4.4 Idealised example continued

We now apply the optimal rotation algorithm to the example of Section 3. We set $\mathbf{v} = (0.4, 0.1, 0.1)$, $v_{tot} = 0.95$, and $\mathbf{W} = \mathbf{\Sigma}_\eta + \mathbf{\Sigma}_e$. One iteration of the algorithm is required to find a basis that satisfies $\mathcal{R}_\mathbf{W}(\mathbf{\Gamma}_q^*, \mathbf{z}) < T$, with $q = 5$.

The reconstruction of \mathbf{z} with this basis, and associated VarMSE plot, are shown in Figure 4. Now, our basis allows us to accurately represent \mathbf{z} with the leading vectors, as the important patterns from low-order eigenvectors have been combined with the leading patterns (hence an additional vector

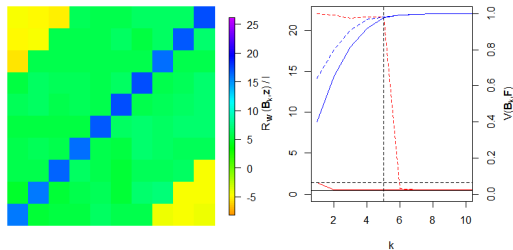


Figure 4: The reconstruction of \mathbf{z} using the truncated basis $\mathbf{\Gamma}_5^*$, and the VarMSE plot for this basis, with the truncated SVD basis given by the red and blue dotted lines.

being required to explain more than 95% of \mathbf{F}_μ).

Performing history matching as before, and using the reconstructions of the original fields rather than the coefficients, we find that 31.5% of χ is now in NROY space (Figure S5). Performing our previous check on the accuracy of the match, we find that no runs consistent with \mathbf{z} have been ruled out.

As we are no longer in the terminal case, we perform probabilistic calibration on the field. The posterior densities found by calibrating on $\mathbf{\Gamma}_q^*$ are shown in Figure S3, with the average simulator output given by samples from this posterior in the first plot of Figure 5. While the samples here are not consistent with \mathbf{z} , as the off-diagonal is too strong, we have been able to identify runs where there is signal on the main diagonal. This is because the rotated basis allows for this direction of the output space to be searched. The limited signal in the important directions from \mathbf{F} has been extracted and used to guide calibration.

We continue the calibration by running a new design within NROY space. This new design should contain more signal in the direction of \mathbf{z} , and hence it should be possible to find a rotation that reduces $\mathcal{R}_{\mathbf{W}}(\cdot, \mathbf{z})$ further than

at the previous wave. We select 60 points from the wave 1 NROY space and run $f(\cdot)$ at these points to give the wave 2 ensemble. We perform a rotation, and emulate and calibrate using the wave 2 ensemble. History matching reduces NROY space to 3.1% of χ (Figure S7). If we instead perform probabilistic calibration, with zero density assigned to regions outside of the wave 1 NROY space, we find the average output field in the 2nd plot of Figure 5 (posteriors in Figure S6).

These results represent a large improvement over performing only one wave. We have ruled out the majority of χ , allowing future runs to be focussed in this region. Probabilistic calibration is more accurate, with samples containing a strong diagonal as with \mathbf{z} .

Repeating the process, our wave 3 ensemble contains patterns more consistent with \mathbf{z} than in previous waves, and hence the truncated SVD basis does not rule out the reconstruction of \mathbf{z} , and no rotation is required. Following emulation for this basis, history matching leads to an NROY space consisting of 2% of χ (Figure S8). Probabilistic calibration (in the wave 2 NROY space) gives the average output in Figure 5 (posteriors in Figure S6), showing that our samples are now consistent with \mathbf{z} .

We strongly advocate performing waves of history matching prior to calibrating probabilistically, removing obviously incorrect regions of χ prior to obtaining more focussed samples in important regions. As was found here and in Salter and Williamson (2016), calibrating probabilistically following waves of history matching gives more accurate results.

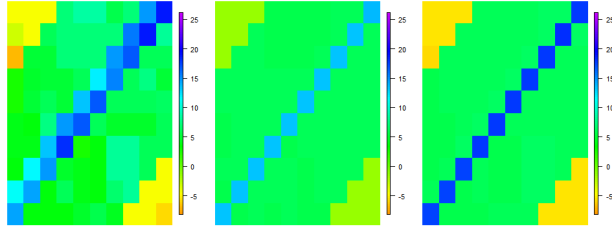


Figure 5: The mean output $f(\mathbf{x})$ for samples of \mathbf{x} from the probabilistic calibration posterior, for the wave 1 rotated basis, the wave 2 rotated basis and the wave 3 SVD basis.

5 Application to tuning climate models

In this section, we will demonstrate that optimal rotation is an important and necessary tool if attempting to perform UQ for climate model tuning. However, as we will discuss, climate model tuning is not a solved problem and it would be of limited value to simply show how calibration with our method can lead to an improvement in one output field over the standard methods, without necessarily improving the whole model or addressing the concerns of the community. We will motivate our discussion using the current Canadian atmosphere model, CanAM4.

CanAM4 is an Atmospheric Global Climate Model, which integrates the primitive equations on a rotating sphere employing a spherical-harmonic spatial discretization truncated triangularly at total wavenumber 63 (T63) with 37 vertical levels spanning the troposphere and stratosphere (von Salzen et al., 2013). CanAM4 has a large number of adjustable, “free”, parameters of which 13 will be varied here. The climatological influence of each set of free parameters is determined from 5-year “present-day” integrations with prescribed sea-surface temperatures and sea-ice. Model output is rep-

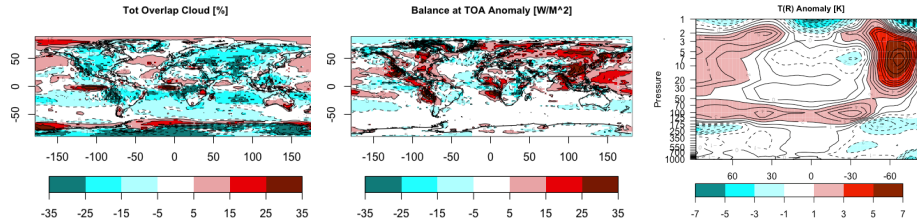


Figure 6: The standard CanAM4 anomaly field for a) CLTO, b) RTMT and c) TA.

resented on the “linear” 128x64 Gaussian grid corresponding to the model’s T63 spectral resolution (37 vertical levels).

There are many output fields that must be checked for consistency with the observed climate when tuning the parameters of a climate model (in the case of CanAM4 there are more than 20). Here we focus on just 3 2D fields: vertical air temperature (TA), the top of the atmosphere radiative balance (RTMT, Wm^{-2}) and the cloud overlap percentage (CLTO). For RTMT and CLTO, the output is given over a longitude-latitude grid, so that $l = 8192$. TA is the temperature averaged over longitude for each latitude and vertical pressure level so that $l = 2368$. There is also a temporal aspect to the output, with monthly values for every grid box; however, we remove this here by averaging over 5 years worth of June, July, August (JJA) outputs. When evaluating and tuning the model, spatial anomaly plots are routinely examined to see how the model compares with observations. An anomaly plot shows the difference between the model and the observations with a blue-white-red colour scale set such that blue is ‘too negative’, white is ‘alright’ and red is ‘too positive’. So, for example, in a temperature anomaly plot, red areas show where the model is too warm (for the modellers) compared to

observations. Figure 6 shows anomaly plots for CLTO, RTMT, and TA for the standard configuration of CanAM4, with the colour scales representing the standard colours used by the modellers when tuning the model.

A goal of tuning is to try to reduce or remove biases that are visible from these plots. Yet equally important is to learn which biases cannot be removed simply by adjusting the model parameters. This is the search for ‘structural errors’ in the model (what statisticians would call model discrepancies). Structural errors indicate that there are flaws with individual parametrisations or with the way they interact that cannot be fixed by tuning. Understanding what these structural errors are so that they might be addressed either as part of this phase of development or for the next is one of the major goals of tuning (Williamson et al., 2015). However, joint estimation of model discrepancy variances and model parameters is not possible without strong prior information (Brynjarsdóttir and O’Hagan, 2014) due to lack of identifiability.

When working with CanAM4 then, our goal is to use history matching with a ‘tolerance to error’ discrepancy variance (Williamson et al., 2015, 2017) that aims to reduce the size of NROY space, so that, ultimately, in a calibration exercise we have strong prior information about \mathbf{x}^* and some structured information on discrepancy. A formal methodology for achieving this is beyond the scope of this paper. However, we will demonstrate that optimal rotation is a crucial component for any attempt of this nature.

We designed 64 runs of CanAM4 varying 13 parameters and using a k -extended Latin Hypercube (Williamson, 2015). Figure 7 shows VarMSE plots for the output fields CLTO, RTMT and TA for this ensemble. The

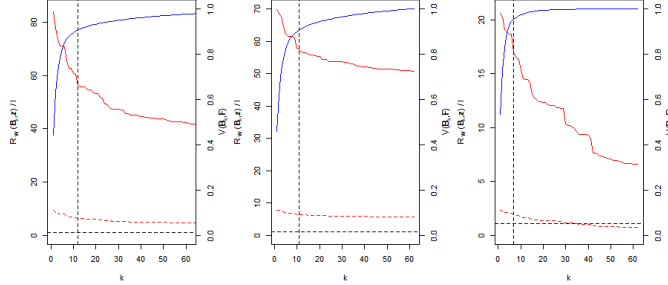


Figure 7: VarMSEplots for a) CLTO b) RTMT and c) TA, with \mathbf{W} based on 1SD (dotted line) and 3SD (solid line). The dotted horizontal line indicates T .

weight matrix \mathbf{W} used for the reconstructions represents our tolerance to model error (we discussed its correspondence to model discrepancy ($\mathbf{W} = \Sigma_{\eta} + \Sigma_{\epsilon}$) in section 4), and the red lines in these plots represent 2 alternatives based on interpreting the colour scales pertaining to the white regions in Figure 6. We assume that the white region represents 3 standard deviations (solid red line) and 1 standard deviation (dashed red line) and set a diagonal \mathbf{W} accordingly. The solid red lines on each plot indicate that we have a terminal case analysis under the small model discrepancy.

The larger discrepancy indicates a terminal case in CLTO and RTMT, and that 35 basis vectors would be enough to adequately reconstruct TA. However, the blue line in the TA plot shows that there is so little ensemble signal on the basis vector coefficients after arguably 20 (or fewer) basis vectors that calibration on 35 basis vectors is not possible. If discrepancy were increased (an operation that involves scaling the red line until it lies below the bound T represented by the dashed horizontal line in the plots), all 3 panels demonstrate that the reconstruction error under SVD decreases

too slowly so that a large number of basis vectors, each with coefficients that are increasingly difficult to emulate due to the decreasing ensemble signal, would be required to avoid a terminal case analysis.

Suppose model discrepancy $\Sigma_\eta \gg \Sigma_e$ so that we can consider $\mathbf{W} = \Sigma_\eta$ in the following. In order to use optimal rotation, we require \mathbf{W} such that $\mathcal{R}_{\mathbf{W}}(\mathbf{B}, \mathbf{z}) < T$, which is not true under our specification above for RTMT and CLTO. If we really believed our Σ_η represented the climate model’s ability to reproduce observed climate, then this indicates that we need a larger ensemble in order to explore the model’s variability. In that case, it may be desirable to follow a procedure like the one we present here to design these runs.

In our case, we believe it is clear that we have misspecified model discrepancy. In fact, we used a place-holder tolerance to error, so this analysis indicates that we are not tolerant enough to model error (at this stage). To explore model discrepancy, we first perform a rotation under the \mathbf{W} given above using the algorithm without step 1 in order to find $\mathcal{R}_{\mathbf{W}}(\mathbf{\Gamma}_q^*, \mathbf{z})$ as close to the reconstruction error of the untruncated SVD basis as possible for small q and whilst retaining emulatability by setting $\mathbf{v} = (0.35, 0.1, 0.1)$ (as 3 rotated vectors is enough). Given this rotation, we then set

$$\Sigma_\eta = \frac{\mathcal{R}_{\mathbf{W}}(\mathbf{\Gamma}_q^*, \mathbf{z})}{b} \mathbf{W}, \quad b = \chi_{l,j}^2 \quad (15)$$

where $j < 0.995$ is a tuning parameter. This ensures that when reconstructed with the new basis, the observations will not be ruled out, and hence we can identify an NROY space likely to contain runs as consistent

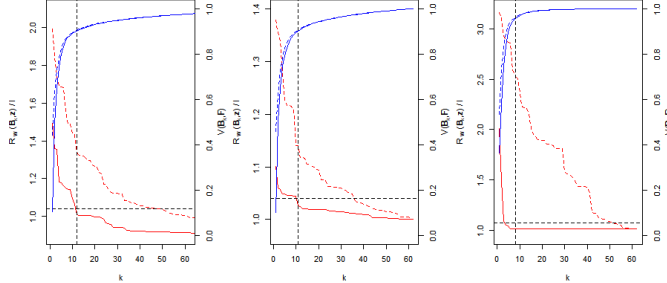


Figure 8: VarMSEplots for CLTO, RTMT and TA, with $\mathbf{W} = \Sigma_{\eta}$, with rotated basis (solid lines) and SVD basis (dotted lines). The dotted horizontal line indicates T .

with \mathbf{z} as possible, given the limited information we have with 64 ensemble members. This has the effect of ‘scaling’ the reconstruction error for the rotated basis seen in Figure 8 below the horizontal dotted line at the point the basis is truncated. For our fields, we set $j = 0.95$ for RTMT, and $j = 0.68$ for the others (as $j = 0.95$ ruled out all of χ for CLTO and TA).

We define NROY space as runs where \mathbf{x} is not ruled out using (3) for each of TA, CLTO and RTMT. This NROY space consists of 0.9% of χ . We then design and run a new 50-member ensemble within this NROY space (discussed in Salter (2017), Section 6.3.5).

Upon inspection of the TA field for this wave 2 ensemble, we observe that every run contains the previously found strong warm bias in the Southern Hemisphere (Figure S9). As our optimal basis choice permitted the search for runs not containing this structural bias, these results are evidence that this may be a structural error. In practice, how much evidence is required before the modellers are convinced that a particular bias is structured or not is a climate modelling decision. Certainly, we could repeat our wave 1

procedure within the current NROY space and run a wave 3 and so on. This has the benefit of increasing the density of points in χ and the accuracy of emulators in key regions of χ , thus insuring against possible ‘spikes’ in the model input space that would correct the bias.

Assuming our modellers were convinced to treat this feature as a structural bias, we demonstrate an approach to include this information within the iterative calibration procedure. We first revisit the specification of the TA discrepancy, selecting the region with the common warm bias shown in Figure S10, deemed to be a structural error and increasing Σ_{η} for the grid boxes in this region. To do this, we set \mathbf{W} as a diagonal matrix with 100 for the grid boxes in this region, and 1s elsewhere on the diagonal.

Using this \mathbf{W} , we select a new basis for TA using the optimal rotation algorithm, and then define the discrepancy Σ_{η} via (15), to ensure that \mathbf{z} is not ruled out (\mathbf{W} reflected our beliefs about the structure, not the magnitude, of Σ_{η}). We re-define the wave 1 NROY space so that it only depends on CLTO and RTMT (consisting of 41.4% of χ) and then include NROY wave 1 runs with the wave 2 ensemble when rotating and building emulators for wave 2. History matching in this new NROY space using the wave 2 bases and emulators leads to an NROY space containing 0.03% of χ . Plots illustrating this NROY space for six of the more active parameters are shown in Figure 9. We see that the regions with the greatest density of points in NROY space are generally found towards the edges of the parameter ranges. From the lower left plots, it is easier to identify relationships between some of the parameters, e.g. CBMF generally needs to be high while UICEFAC needs to be towards the centre of its allowable range.

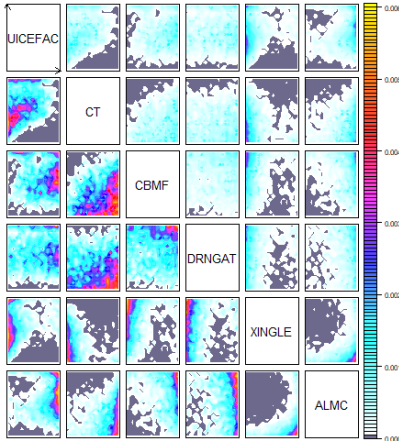


Figure 9: Plot showing the composition of the wave 2 NROY space for 6 of the parameters of CanAM4. For each cell of a pairwise plot, a large sample is taken over the remaining parameters and the proportion of space that is not ruled out is calculated. The lower left gives the same plots, with scales set for each individual plot to show more structure.

The calibration of climate models, or even simply the search for structural biases is a massive undertaking, and a full tuning is well-beyond the scope of this paper. Each small ensemble of CanAM4 required 2 days of super-computer time to run and, in reality, the modellers routinely check over 20 spatial fields (and a host of other metrics) when tuning the model. UQ can help with the tuning procedure in providing tools (emulators) that allow χ to be explored much more quickly than is currently possible at the modelling centres. However, as this application has demonstrated, using the off-the-shelf methods based on the SVD basis does not work for tuning in general. It did not work for the 3 fields we showed here, nor have the authors ever found climate model output for which the problems we identified here were not present. Our application demonstrates the optimal rotation algorithm as an effective solution to quickly find bases without these issues

for calibration.

6 Discussion

In this paper, we highlighted the issue of terminal case analyses for the calibration of computer models. A terminal case analysis occurs when the prior assessment of model discrepancy is inconsistent with the computer simulator’s ability to mimic reality and leads either to useless and incorrect posterior distributions (using the fully Bayesian procedure) or ruling out all of parameter space (using history matching). We showed that even when the prior assessment of model discrepancy is not inconsistent with the ability of the simulator, dimension-reduction of spatial output using the ensemble derived principal components (the SVD basis) often leads to a terminal case analysis.

We proposed a rotation of the SVD basis to highlight and incorporate important low-signal patterns that may be contained in the original SVD basis, giving a new basis that avoids the terminal case when this is possible. We then presented an efficient algorithm for optimal rotation, guaranteeing to avoid the terminal case when the model discrepancy allows, whilst ensuring enough signal on leading basis vectors to permit the fitting of emulators. We proved that our algorithm gives a valid rotation of the original basis, and established a fast test to see whether a given ensemble of model runs and discrepancy specification automatically leads to a terminal case analysis prior to rotation.

We demonstrated the efficacy of our method using an idealised application, and showed that it scaled up to the important case of spatial output

for state-of-the-art climate models. Our application highlighted the issue of the terminal case for climate model analyses and showed the problems with using SVD in practice. We applied history matching for 2 waves to CanAM4 and showed how, combined with optimal rotation, we can begin to distinguish between what the modellers term ‘structural errors’ and ‘tuning errors’.

A purely methodological UQ approach for tuning climate models does not exist. It may be tempting, for UQ practitioners who are not familiar with climate models, to claim that calibration of computer simulators is a ‘solved’ problem and that ‘all’ that is required is for the modellers to specify their model discrepancy. We believe that the challenge for model tuning lies in the understanding of this elusive quantity. For the statistical community, rather than focussing on developing comprehensive methods for calibrating climate models automatically, this should mean engaging with modellers to develop robust tools and methods to help identify and understand these errors. This type of approach would have obvious implications for tuning, but would also feed into model development as it becomes better understood which parameters control various biases and therefore which parameterisations need particular attention during the next development cycle.

References

Bayarri, M., J. Berger, J. Cafeo, G. Garcia-Donato, F. Liu, J. Palomo, R. Parthasarathy, R. Paulo, J. Sacks, and D. Walsh (2007). Computer model validation with functional output. *The Annals of Statistics*, 1874–

1906.

Björck, Å. (1967). Solving linear least squares problems by Gram-Schmidt orthogonalization. *BIT Numerical Mathematics* 7(1), 1–21.

Björck, Å. (1994). Numerics of Gram-Schmidt orthogonalization. *Linear Algebra and Its Applications* 197, 297–316.

Brynjarsdóttir, J. and A. O’Hagan (2014). Learning about physical parameters: The importance of model discrepancy. *Inverse Problems* 30(11), 114007.

Chang, W., P. J. Applegate, M. Haran, and K. Keller (2014). Probabilistic calibration of a Greenland Ice Sheet model using spatially-resolved synthetic observations: toward projections of ice mass loss with uncertainties. *Geoscientific Model Development Discussions* 7(2), 1905–1931.

Chang, W., M. Haran, P. Applegate, and D. Pollard (2016). Calibrating an ice sheet model using high-dimensional binary spatial data. *Journal of the American Statistical Association* 111(513), 57–72.

Chen, H., J. L. Loeppky, J. Sacks, W. J. Welch, et al. (2016). Analysis Methods for Computer Experiments: How to Assess and What Counts? *Statistical Science* 31(1), 40–60.

Collins, M., S.-I. An, W. Cai, A. Ganachaud, E. Guilyardi, F.-F. Jin, M. Jochum, M. Lengaigne, S. Power, A. Timmermann, et al. (2010). The impact of global warming on the tropical pacific ocean and el niño. *Nature Geoscience* 3(6), 391–397.

- Conti, S. and A. O’Hagan (2010). Bayesian emulation of complex multi-output and dynamic computer models. *Journal of statistical planning and inference* 140(3), 640–651.
- Craig, P. S., M. Goldstein, A. Seheult, and J. Smith (1996). Bayes linear strategies for matching hydrocarbon reservoir history. *Bayesian statistics* 5, 69–95.
- Goldstein, M. and J. Rougier (2009). Reified bayesian modelling and inference for physical systems. *Journal of Statistical Planning and Inference* 139(3), 1221–1239.
- Gu, M., J. O. Berger, et al. (2016). Parallel partial Gaussian process emulation for computer models with massive output. *The Annals of Applied Statistics* 10(3), 1317–1347.
- Harris, G., D. Sexton, B. Booth, M. Collins, J. Murphy, and M. Webb (2006). Frequency distributions of transient regional climate change from perturbed physics ensembles of general circulation model simulations. *Climate Dynamics* 27(4), 357–375.
- Haylock, R. and A. O’Hagan (1996). On inference for outputs of computationally expensive algorithms with uncertainty on the inputs. *Bayesian statistics* 5, 629–637.
- Higdon, D., J. Gattiker, B. Williams, and M. Rightley (2008). Computer model calibration using high-dimensional output. *Journal of the American Statistical Association* 103(482).

- Hourdin, F., T. Mauritsen, A. Gettelman, J.-C. Golaz, V. Balaji, Q. Duan, D. Folini, D. Ji, D. Klocke, Y. Qian, et al. (2017). The art and science of climate model tuning. *Bulletin of the American Meteorological Society* 98(3), 589–602.
- Kaufman, C. G., D. Bingham, S. Habib, K. Heitmann, and J. A. Frieman (2011). Efficient emulators of computer experiments using compactly supported correlation functions, with an application to cosmology. *The Annals of Applied Statistics* 5(4), 2470–2492.
- Kennedy, M. C. and A. O’Hagan (2001). Bayesian calibration of computer models. *Journal of the Royal Statistical Society: Series B (Statistical Methodology)* 63(3), 425–464.
- Kuttler, K. (2012). *Linear algebra: theory and applications*. The Saylor Foundation.
- Mauritsen, T., B. Stevens, E. Roeckner, T. Crueger, M. Esch, M. Giorgetta, H. Haak, J. Jungclaus, D. Klocke, D. Matei, et al. (2012). Tuning the climate of a global model. *Journal of Advances in Modeling Earth Systems* 4(3).
- Meehl, G. A., G. J. Boer, C. Covey, M. Latif, and R. J. Stouffer (2000). The coupled model intercomparison project (cmip). *Bulletin of the American Meteorological Society* 81(2), 313–318.
- Murnaghan, F. D. (1962). *The unitary and rotation groups*, Volume 3. Spartan books.

- Pollard, D., W. Chang, M. Haran, P. Applegate, and R. DeConto (2016). Large ensemble modeling of the last deglacial retreat of the west antarctic ice sheet: comparison of simple and advanced statistical techniques. *Geoscientific Model Development* 9(5), 1697–1723.
- Pukelsheim, F. (1994). The three sigma rule. *The American Statistician* 48(2), 88–91.
- Sacks, J., W. J. Welch, T. J. Mitchell, and H. P. Wynn (1989). Design and analysis of computer experiments. *Statistical science*, 409–423.
- Salter, J. M. (2017). *Uncertainty quantification for spatial field data using expensive computer models: refocussed Bayesian calibration with optimal projection*. Ph. D. thesis, University of Exeter.
- Salter, J. M. and D. Williamson (2016). A comparison of statistical emulation methodologies for multi-wave calibration of environmental models. *Environmetrics* 27(8), 507–523.
- Scaife, A. A., T. Spanghel, D. R. Fereday, U. Cubasch, U. Langematz, H. Akiyoshi, S. Bekki, P. Braesicke, N. Butchart, M. P. Chipperfield, et al. (2012). Climate change projections and stratosphere–troposphere interaction. *Climate Dynamics* 38(9-10), 2089–2097.
- Screen, J. A. and D. Williamson (2017). Ice-free arctic at 1.5 [deg] c? *Nature Climate Change* 7(4), 230–231.
- Sexton, D. M., J. M. Murphy, M. Collins, and M. J. Webb (2011). Mul-

tivariate probabilistic projections using imperfect climate models part I: outline of methodology. *Climate dynamics* 38(11-12), 2513–2542.

Stocker, T. F., D. Qin, G.-K. Plattner, M. Tignor, S. K. Allen, J. Boschung, A. Nauels, Y. Xia, B. Bex, and B. Midgley (2013). Ipcc, 2013: climate change 2013: the physical science basis. contribution of working group i to the fifth assessment report of the intergovernmental panel on climate change.

Vernon, I., M. Goldstein, and R. G. Bower (2010). Galaxy formation: a Bayesian uncertainty analysis. *Bayesian Analysis* 5(4), 619–669.

von Salzen, K., J. F. Scinocca, N. A. McFarlane, J. Li, J. N. Cole, D. Plummer, D. Verseghy, M. C. Reader, X. Ma, M. Lazare, et al. (2013). The Canadian fourth generation atmospheric global climate model (CanAM4). Part I: representation of physical processes. *Atmosphere-Ocean* 51(1), 104–125.

Wilkinson, R. D. (2010). Bayesian calibration of expensive multivariate computer experiments. *Large-Scale Inverse Problems and Quantification of Uncertainty, Ser. Comput. Stat., edited by LT Biegler et al*, 195–216.

Williamson, D. (2015). Exploratory ensemble designs for environmental models using k-extended Latin Hypercubes. *Environmetrics* 26(4), 268–283.

Williamson, D., A. T. Blaker, C. Hampton, and J. Salter (2015). Identifying and removing structural biases in climate models with history matching. *Climate Dynamics* 45(5-6), 1299–1324.

Williamson, D., M. Goldstein, L. Allison, A. Blaker, P. Challenor, L. Jackson, and K. Yamazaki (2013). History matching for exploring and reducing climate model parameter space using observations and a large perturbed physics ensemble. *Climate dynamics* 41(7-8), 1703–1729.

Williamson, D., M. Goldstein, and A. Blaker (2012). Fast linked analyses for scenario-based hierarchies. *Journal of the Royal Statistical Society: Series C (Applied Statistics)* 61(5), 665–691.

Williamson, D. B., A. T. Blaker, and B. Sinha (2017). Tuning without over-tuning: parametric uncertainty quantification for the nemo ocean model. *Geoscientific Model Development* 10(4), 1789.

Supplemental Material: Uncertainty quantification for spatio-temporal computer models with calibration-optimal bases

S1 Idealised example

The spatial idealised example $f(\mathbf{x})$ gives output over a 10×10 field, with 6 input parameters each taking values in $[-1, 1]$:

$$\begin{aligned}
 f(\mathbf{x}) = & 3(10x_2^2\varphi_2 + 5x_3^2\varphi_2 + (x_3 + 1.5x_1x_2)\varphi_3 + 2x_2\varphi_4 + x_3x_1\varphi_5 + (x_2x_1)\varphi_6 + x_2^3\varphi_7 \\
 & + (x_2 + x_3)^2\varphi_8 + 2) + 1.5\pi_N(x_4, 0.2, 0.1^2)\varphi_1 \frac{x_5}{1.3 + x_6} + \Psi_{10 \times 10}(0, 0.05^2)
 \end{aligned}
 \tag{S1}$$

where $\pi_N(x_4, 0.2, 0.1^2)$ denotes the density function of the Normal distribution with mean 0.2 and variance 0.1^2 , and $\Psi_{10 \times 10}(0, 0.05^2)$ denotes sampling from a Normal distribution with mean zero and variance 0.05^2 , independently for each box in a 10×10 grid. The basis vectors used in this definition, $(\varphi_1, \dots, \varphi_8)$, are shown in Figure S1. φ_1 represents the pattern that is most similar to the observations \mathbf{z} , and φ_2 represents the biased version of the observations, most prevalent in sampled ensembles.

The value of \mathbf{x}^* is set as

$$\mathbf{x}^* = (0.7, 0.01, 0.01, 0.25, 0.8, -0.9)$$

with the observed field, \mathbf{z} , given by adding a sample from $N(\mathbf{0}, \Sigma_e)$ to $f(\mathbf{x}^*)$, to represent observation error. We define Σ_e using the Gaussian correlation

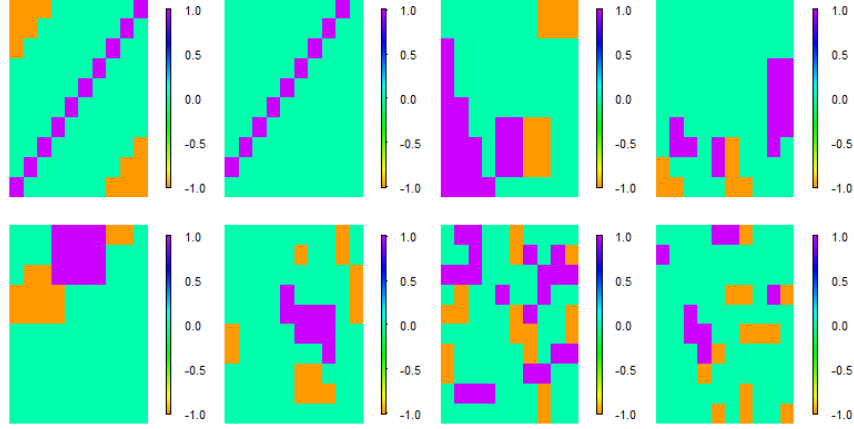


Figure S1: The 8 orthogonal basis vectors used in the definition of the spatial toy function, with φ_1 the top left plot, φ_2 to the right of this, etc.

function, with the input parameters treated as the spatial coordinates of the 10×10 grid, $s_i = (a_i, b_i)$. The correlation length for each dimension is set equal to 1, the nugget parameter set at 0, and the common variance multiplier set equal to 1, so that the i, j^{th} entry of Σ_e is

$$\Sigma_e^{ij} = \exp\{-(a_i - a_j)^2 - (b_i - b_j)^2\} \quad (\text{S2})$$

Discrepancy

The discrepancy is modelled as a zero mean l -dimensional Gaussian process:

$$\boldsymbol{\eta} \sim \text{N}(\mathbf{0}, \Sigma_\eta)$$

For Σ_η , we define variances v_i for the discrepancy for each grid box. Hence, the $(i, j)^{th}$ entry of the variance matrix is

$$\Sigma_\eta^{ij} = v_i v_j C(s_i, s_j)$$

where $C(\cdot, \cdot)$ is a correlation function that gives the correlation between locations s_i and s_j . Therefore, the parameters that need to be defined to complete the specification are v_1, \dots, v_l and the correlation length parameters of $C(\cdot, \cdot)$.

For our function, the most important aspect of the output is the signal on the main diagonal, and spatial fields where this is accurate, but perhaps aren't exactly correct elsewhere, should not be ruled out. Let the indices for the grid boxes on the diagonal be contained in the set S . Then the discrepancy variances v_i are specified via

$$v_i = \begin{cases} w_1 & \text{if } i \in S \\ w_2 & \text{otherwise} \end{cases}$$

w_1 is set equal to 0.1, and w_2 to 1, i.e. the output can be ‘more wrong’ outside of S . The specification of the discrepancy is completed by using the squared exponential as the correlation function, with the correlation length parameters both set equal to 1. Figure S2 shows the true NROY space given Σ_e and Σ_η .

S1.1 Probabilistic calibration for the SVD basis

The dotted lines on Figure S3 show the resulting densities when the truncated SVD basis, Γ_4 , is used to calibrate probabilistically on the field, for the input parameters x_1, \dots, x_5 , and the ratio $r = x_5/(1.3 + x_6)$. There are peaks of density away from the true values (\mathbf{x}^* , as shown by the red vertical lines), particularly for x_3 and r . For x_4 , the parameter that controls the

strength of the main diagonal, the posterior density is relatively flat across the entire range of x_4 .

By sampling from these posteriors and evaluating the idealised example at these parameter choices, we can check whether calibration with the truncated SVD basis has simply highlighted another region of parameter space that is ‘close’ to \mathbf{z} . 16 samples are shown in Figure S4, demonstrating that the results suggest it is not possible to remove the off-diagonal pattern that was dominant in the ensemble.

S1.2 Calibration with the rotated bases

The solid lines in Figure S3 show the posterior distributions for x_1, \dots, x_5 and r when the wave 1 rotated basis is used for probabilistic calibration, showing improvements (compared to the SVD basis) for x_4 and r .

At wave 2, there are peaks of density at or near to the true parameter values for all but x_5 and x_6 , as shown by the solid lines in Figure S6. The dotted lines in this plot show the wave 3 posteriors. Although the peaks for x_2 , x_3 and x_4 are not as large, this wave offers an improvement for r (important for the strength of the main diagonal) and x_1 (as this parameter has no effect on the main or off-diagonal, a flat posterior is more accurate).

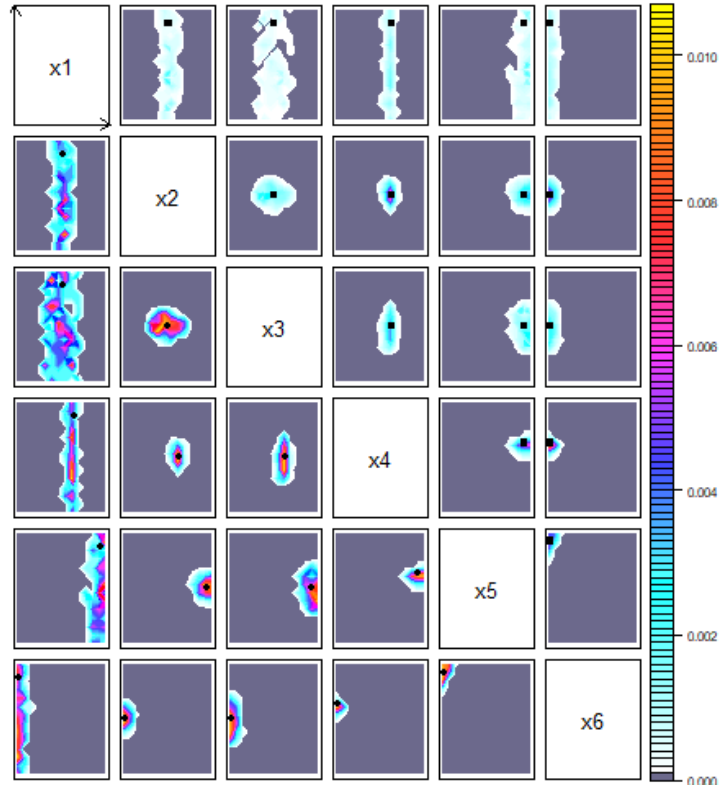


Figure S2: Density plot of the true NROY space (i.e. no emulation involved), for each pair of parameters. For each cell in a pairwise plot, the remaining parameters are averaged over, and the proportion in NROY space for each pair is plotted. The axes are reversed for the lower left plots, with the colour scale set individually for each of these plots. The black point corresponds to x^* .

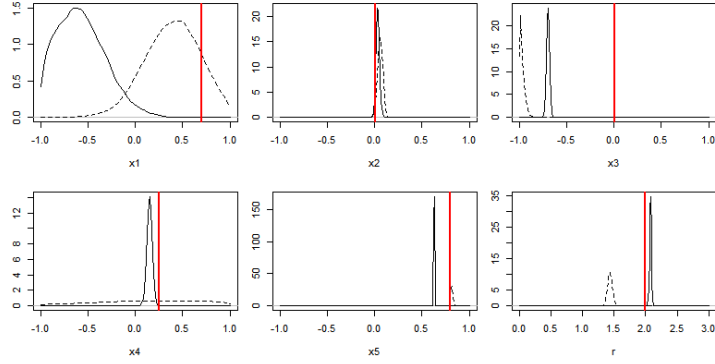


Figure S3: The posterior distributions for x_1, \dots, x_5 and r , when probabilistic calibration is performed on the field using the SVD basis derived from the wave 1 ensemble, Γ_4 (dotted lines), and the wave 1 rotated basis (solid lines). The red vertical lines indicate the true value of \mathbf{x}^* .

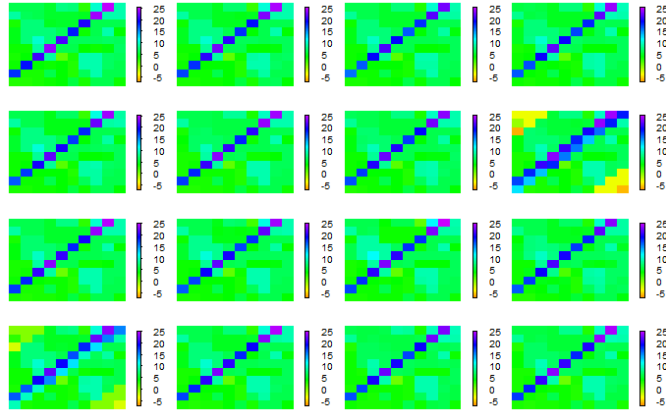


Figure S4: $f(\mathbf{x})$ at 16 samples of \mathbf{x} from the calibration posterior distribution, using the SVD basis Γ_4 for projection and emulation.

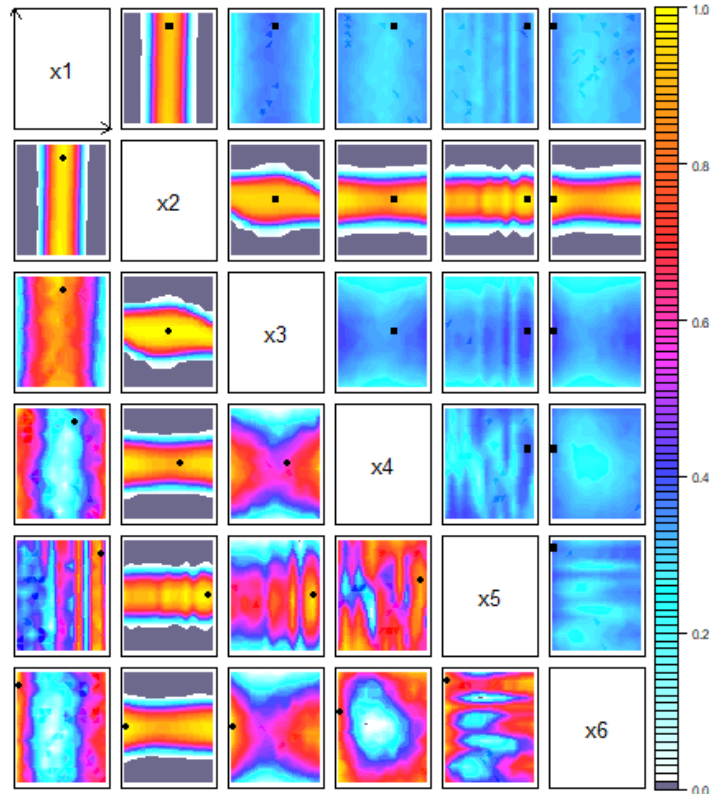


Figure S5: Density plot for the wave 1 NROY space defined using the rotated basis, for each pair of parameters. The remaining parameters are averaged over for each plot, and the proportion in NROY space for each pair is plotted. The axes are reversed for the lower left plots, and the colour scales set differently. The black point corresponds to \mathbf{x}^* .

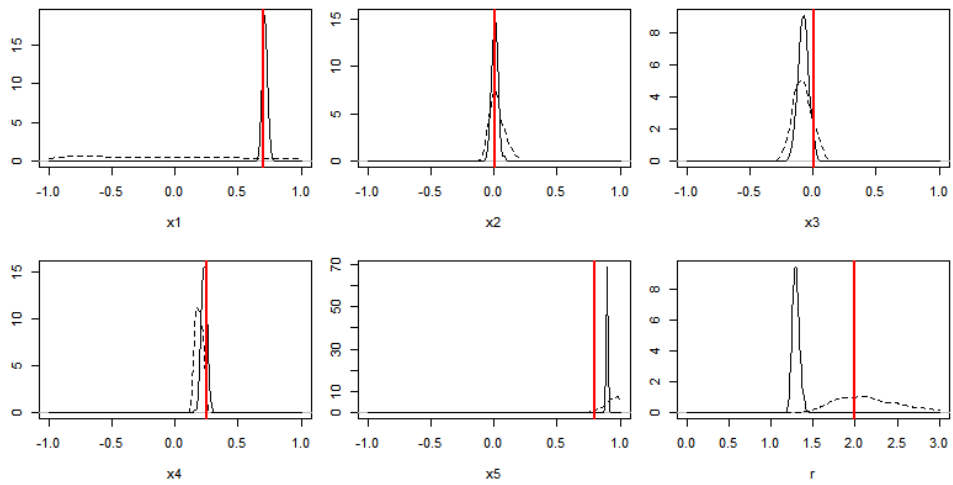


Figure S6: The posterior distributions for x_1, \dots, x_5 and r , at wave 2 (solid lines) and wave 3 (dotted lines). The red vertical lines indicate the true value of \mathbf{x}^* .

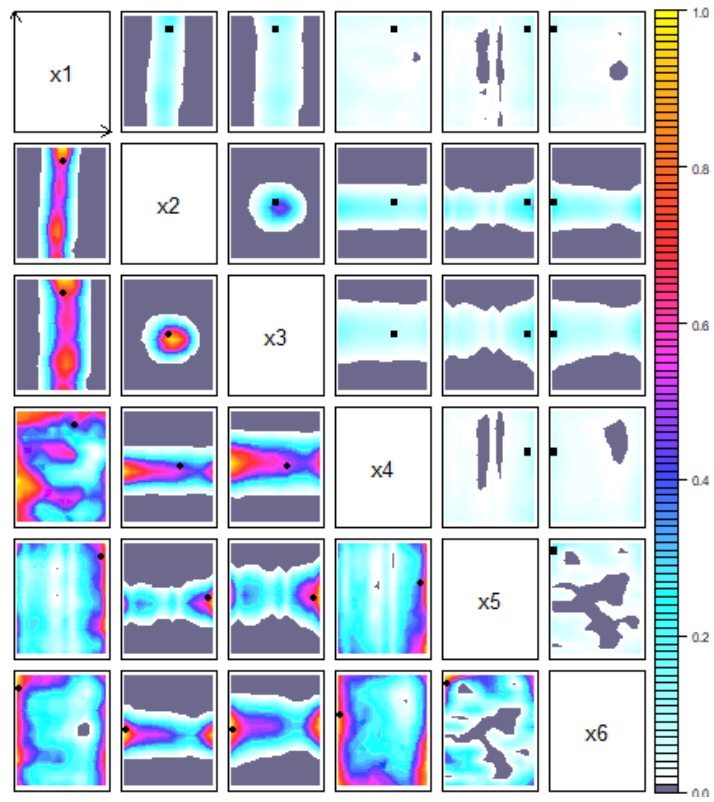


Figure S7: Density plot for the wave 2 NROY space for each pair of parameters.

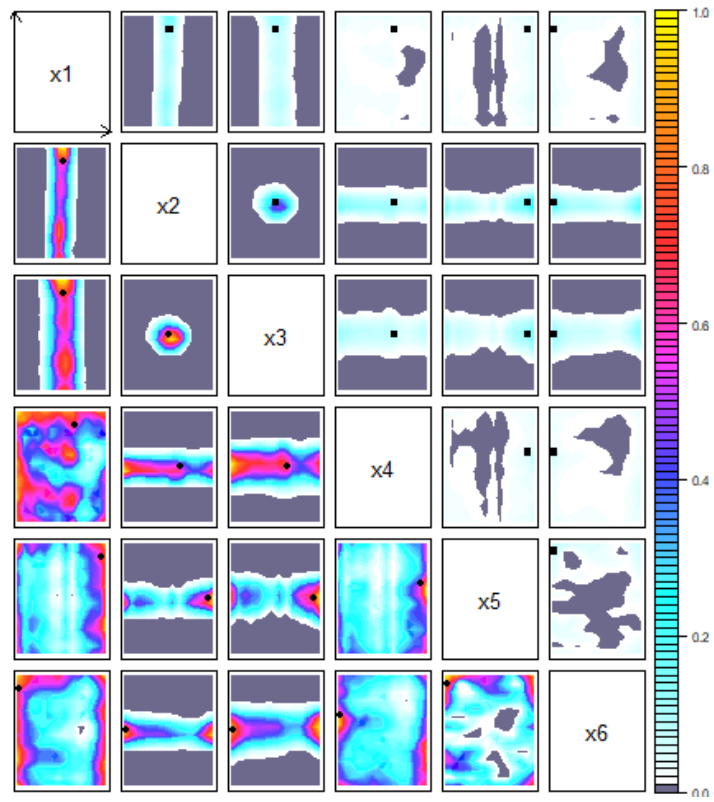


Figure S8: Density plot for the wave 3 NROY space for each pair of parameters.

S2 Proofs

Result 1 (Invariance of $\mathcal{R}_{\mathbf{W}}(\cdot, \cdot)$ to rotation). *For a rotation matrix $\mathbf{\Lambda}$ of dimension $k \times k$, and a set of basis vectors $\mathbf{B} = (\mathbf{b}_1, \dots, \mathbf{b}_n)$, we have*

$$\mathcal{R}_{\mathbf{W}}(\mathbf{B}_k, \mathbf{z}) = \mathcal{R}_{\mathbf{W}}(\mathbf{B}_k \mathbf{\Lambda}, \mathbf{z}), \quad k = 1, \dots, n$$

Proof. The reconstruction error for the rotated basis can be written as

$$\begin{aligned} \mathcal{R}_{\mathbf{W}}(\mathbf{B}_k \mathbf{\Lambda}, \mathbf{z}) &= \|\mathbf{z} - \mathbf{B}_k \mathbf{\Lambda} ((\mathbf{B}_k \mathbf{\Lambda})^T \mathbf{B}_k \mathbf{\Lambda})^{-1} (\mathbf{B}_k \mathbf{\Lambda})^T \mathbf{z}\|_{\mathbf{W}} \\ &= \|\mathbf{z} - \mathbf{B}_k \mathbf{\Lambda} (\mathbf{\Lambda}^T \mathbf{B}_k^T \mathbf{B}_k \mathbf{\Lambda})^{-1} \mathbf{\Lambda}^T \mathbf{B}_k^T \mathbf{z}\|_{\mathbf{W}} \end{aligned}$$

By the definition of rotation matrices, $\mathbf{\Lambda}$ is invertible, with $\mathbf{\Lambda}^T = \mathbf{\Lambda}^{-1}$. Furthermore, $\mathbf{\Lambda}^T \mathbf{B}_k^T \mathbf{B}_k$ is a square matrix, and is invertible ($\mathbf{B}_k^T \mathbf{B}_k$ is non-singular as \mathbf{B}_k is a basis, so none of the columns are linear combinations of each other, i.e. \mathbf{B}_k has rank k), so that the identity $(\mathbf{C}\mathbf{D})^{-1} = \mathbf{D}^{-1}\mathbf{C}^{-1}$ for \mathbf{C}, \mathbf{D} both $k \times k$ invertible matrices can be applied:

$$\begin{aligned} &= \|\mathbf{z} - \mathbf{B}_k \mathbf{\Lambda} \mathbf{\Lambda}^{-1} (\mathbf{\Lambda}^T \mathbf{B}_k^T \mathbf{B}_k)^{-1} \mathbf{\Lambda}^T \mathbf{B}_k^T \mathbf{z}\|_{\mathbf{W}} \\ &= \|\mathbf{z} - \mathbf{B}_k (\mathbf{B}_k^T \mathbf{B}_k)^{-1} (\mathbf{\Lambda}^T)^{-1} \mathbf{\Lambda}^T \mathbf{B}_k^T \mathbf{z}\|_{\mathbf{W}} \\ &= \|\mathbf{z} - \mathbf{B}_k (\mathbf{B}_k^T \mathbf{B}_k)^{-1} \mathbf{B}_k^T \mathbf{z}\|_{\mathbf{W}} \\ &= \mathcal{R}_{\mathbf{W}}(\mathbf{B}_k, \mathbf{z}) \end{aligned}$$

where the same identity has been applied a second time, with $\mathbf{C} = \mathbf{\Lambda}^T$ and $\mathbf{D} = \mathbf{B}_k^T \mathbf{B}_k$, to give the result. \square

Prior to proving the theorem, we require 2 further results:

Result S2 (Orthogonality of the residual basis). *The residual basis, \mathbf{B}_ϵ , calculated from \mathbf{F}_μ and \mathbf{B}_p , is orthogonal to \mathbf{B}_p .*

Proof. First, we show that the columns of the residual ensemble, \mathbf{F}_ϵ , are each orthogonal to the columns of \mathbf{B}_p :

$$\begin{aligned}
\mathbf{B}_p^T \mathbf{F}_\epsilon &= \mathbf{B}_p^T (\mathbf{F}_\mu - \mathbf{B}_p (\mathbf{B}_p^T \mathbf{B}_p)^{-1} \mathbf{B}_p^T \mathbf{F}_\mu) \\
&= \mathbf{B}_p^T \mathbf{F}_\mu - (\mathbf{B}_p^T \mathbf{B}_p) (\mathbf{B}_p^T \mathbf{B}_p)^{-1} \mathbf{B}_p^T \mathbf{F}_\mu \\
&= \mathbf{B}_p^T \mathbf{F}_\mu - \mathbf{B}_p^T \mathbf{F}_\mu \\
&= \mathbf{0}
\end{aligned}$$

The result is a $p \times n$ zero matrix, so that each of the vectors of \mathbf{B}_p are orthogonal with the vectors of \mathbf{F}_ϵ . Using this, and the definition of the singular value decomposition of \mathbf{F}_ϵ , we show that the residual basis, \mathbf{B}_ϵ , is orthogonal to \mathbf{B}_p :

$$\begin{aligned}
\mathbf{F}_\epsilon^T &= \mathbf{U} \mathbf{\Sigma} \mathbf{V}^T \\
\implies \mathbf{F}_\epsilon^T &= \mathbf{U} \mathbf{\Sigma} \mathbf{B}_\epsilon^T
\end{aligned}$$

where \mathbf{U} is an orthonormal $n \times n$ matrix, $\mathbf{\Sigma}$ is a diagonal $n \times n$ matrix, and $\mathbf{V} = \mathbf{B}_\epsilon$ is an $l \times n$ matrix with orthonormal columns, so that $\mathbf{B}_\epsilon^T \mathbf{B}_\epsilon = \mathbb{I}_n$. Taking the transpose and multiplying on the right by \mathbf{U} gives

$$\begin{aligned}
\implies \mathbf{F}_\epsilon &= \mathbf{B}_\epsilon \mathbf{\Sigma}^T \mathbf{U}^T \\
\implies \mathbf{F}_\epsilon \mathbf{U} &= \mathbf{B}_\epsilon \mathbf{\Sigma}^T \mathbf{U}^T \mathbf{U} \\
\implies \mathbf{B}_p^T \mathbf{F}_\epsilon \mathbf{U} &= \mathbf{B}_p^T \mathbf{B}_\epsilon \mathbf{\Sigma}^T
\end{aligned}$$

where the orthonormality of \mathbf{U} has been used, and the equation has been multiplied on the left by \mathbf{B}_p^T . From above, $\mathbf{B}_p^T \mathbf{F}_\epsilon = \mathbf{0}$, and hence

$$\implies \mathbf{B}_p^T \mathbf{B}_\epsilon \boldsymbol{\Sigma}^T = \mathbf{0}$$

\mathbf{B}_ϵ has dimension $l \times n$, and $\boldsymbol{\Sigma}$ has dimension $n \times n$, due to the dimension of the residual ensemble. However, the final $(p + 1)$ eigenvalues contained on the diagonal of $\boldsymbol{\Sigma}$ are zero (due to the degrees of freedom removed by the ensemble mean and the p chosen patterns), and hence only the first $(n - p - 1)$ columns of \mathbf{B}_ϵ are of interest, as no ensemble variability is explained by the final $(p + 1)$ columns. Discarding columns associated with zero eigenvalues (as the basis would always be truncated before zero-eigenvalue vectors are included), and using that $\boldsymbol{\Sigma}$ is diagonal, the final step is

$$\implies \mathbf{B}_p^T \mathbf{B}_\epsilon = \mathbf{0}$$

and hence the vectors of the residual basis are orthogonal to the chosen basis vectors, as expected. \square

From this result, we have that the basis vector selected at step k of the algorithm, $\boldsymbol{\gamma}_k^*$, is orthogonal to those previously selected, $\boldsymbol{\Gamma}_{k-1}^* = (\boldsymbol{\gamma}_1^*, \dots, \boldsymbol{\gamma}_{k-1}^*)$, i.e.

$$(\boldsymbol{\Gamma}_{k-1}^*)^T \boldsymbol{\gamma}_k^* = (\boldsymbol{\Gamma}_{k-1}^*)^T \mathbf{B}_\epsilon \boldsymbol{\lambda}_k = \mathbf{0}$$

Result S3. *When \mathbf{B} is a basis for \mathbf{F}_μ , we can write $\mathbf{B}_\epsilon = \mathbf{B}\boldsymbol{\Lambda}_\epsilon$ for square $\boldsymbol{\Lambda}_\epsilon$, i.e. the residual basis contains linear combinations of the vectors of \mathbf{B} .*

Proof. From the definition of SVD, we have

$$\mathbf{F}_\epsilon^T = \mathbf{U}_\epsilon \boldsymbol{\Sigma}_\epsilon \mathbf{B}_\epsilon^T$$

for an orthonormal matrix \mathbf{U}_ϵ , and diagonal $\boldsymbol{\Sigma}_\epsilon$. As \mathbf{B} is a basis for \mathbf{F}_μ , each member of \mathbf{F}_μ can be written as a linear combination of the columns of \mathbf{B} , i.e. $\mathbf{F}_\mu = \mathbf{B}\boldsymbol{\Lambda}_\mu$, for an $n \times n$ matrix $\boldsymbol{\Lambda}_\mu$. Therefore, at step k we have

$$\begin{aligned} \mathbf{B}_\epsilon \boldsymbol{\Sigma}_\epsilon \mathbf{U}_\epsilon^T &= \mathbf{F}_\mu - \boldsymbol{\Gamma}_k^* (\boldsymbol{\Gamma}_k^*)^T \mathbf{F}_\mu \\ \implies \mathbf{B}_\epsilon &= (\mathbf{B}\boldsymbol{\Lambda}_\mu - \boldsymbol{\Gamma}_k^* (\boldsymbol{\Gamma}_k^*)^T \mathbf{B}\boldsymbol{\Lambda}_\mu) \mathbf{U}_\epsilon \boldsymbol{\Sigma}_\epsilon^{-1} \end{aligned}$$

Let $k = 1$, hence we can write $\boldsymbol{\Gamma}_1^* = \mathbf{B}\boldsymbol{\Lambda}_1^*$ (as the first new vector is a linear combination of \mathbf{B} by construction). Therefore,

$$\begin{aligned} \mathbf{B}_\epsilon &= (\mathbf{B}\boldsymbol{\Lambda}_\mu - \mathbf{B}\boldsymbol{\Lambda}_k^* (\mathbf{B}\boldsymbol{\Lambda}_k^*)^T \mathbf{B}\boldsymbol{\Lambda}_\mu) \mathbf{U}_\epsilon \boldsymbol{\Sigma}_\epsilon^{-1} \\ &= \mathbf{B}(\boldsymbol{\Lambda}_\mu - \boldsymbol{\Lambda}_k^* (\boldsymbol{\Lambda}_k^*)^T \boldsymbol{\Lambda}_\mu) \mathbf{U}_\epsilon \boldsymbol{\Sigma}_\epsilon^{-1} = \mathbf{B}\boldsymbol{\Lambda}_\epsilon \end{aligned} \tag{S3}$$

with $\boldsymbol{\Lambda}_\epsilon = (\boldsymbol{\Lambda}_\mu - \boldsymbol{\Lambda}_k^* (\boldsymbol{\Lambda}_k^*)^T \boldsymbol{\Lambda}_\mu) \mathbf{U}_\epsilon \boldsymbol{\Sigma}_\epsilon^{-1}$. Hence, at step $k = 2$, we have (finding a linear combination of the residual basis)

$$\boldsymbol{\gamma}_2^* = \mathbf{B}_\epsilon \boldsymbol{\lambda}_2 = \mathbf{B}\boldsymbol{\Lambda}_\epsilon \boldsymbol{\lambda}_2 = \mathbf{B}\tilde{\boldsymbol{\lambda}}_2$$

i.e. the second new basis vector (and hence any subsequent k^{th} vector) is a linear combination of \mathbf{B} , and we can write $\boldsymbol{\Gamma}_k^* = \mathbf{B}\boldsymbol{\Lambda}_k^*$ for an $n \times k$ matrix $\boldsymbol{\Lambda}_k^*$, and (S3) holds for the residual basis at step k . \square

S2.1 Proof of Theorem 1

Theorem 1. $\mathbf{\Gamma}^*$ in step 3 of the optimal rotation algorithm is an orthogonal rotation of \mathbf{B} .

Proof. Assume that we have performed k iterations of the algorithm, resulting in the basis

$$\mathbf{\Gamma}^* = (\gamma_1^*, \dots, \gamma_k^*, [\mathbf{B}_\epsilon]_{n-k}) \quad (\text{S4})$$

First, using $\mathbf{B}_\epsilon = \mathbf{B}\mathbf{\Lambda}_\epsilon$ and $\gamma_j^* = \mathbf{B}\tilde{\lambda}_j$ (Result S3), we rewrite (S4) as

$$\mathbf{\Gamma}^* = (\mathbf{B}\tilde{\lambda}_1, \dots, \mathbf{B}\tilde{\lambda}_k, [\mathbf{B}\mathbf{\Lambda}_\epsilon]_{n-k}) = \mathbf{B}(\tilde{\lambda}_1, \dots, \tilde{\lambda}_k, [\mathbf{\Lambda}_\epsilon]_{n-k}) = \mathbf{B}\mathbf{\Lambda}.$$

We now show that $\mathbf{\Lambda}$ is a rotation matrix, i.e. $\mathbf{\Lambda}^T \mathbf{\Lambda} = \mathbb{I}_n$. We have

$$\mathbf{\Lambda}^T \mathbf{\Lambda} = \begin{pmatrix} \tilde{\lambda}_1^T \tilde{\lambda}_1 & \tilde{\lambda}_1^T \tilde{\lambda}_2 & \dots & \tilde{\lambda}_1^T [\mathbf{\Lambda}_\epsilon]_{n-k} \\ \tilde{\lambda}_2^T \tilde{\lambda}_1 & \tilde{\lambda}_2^T \tilde{\lambda}_2 & \dots & \tilde{\lambda}_2^T [\mathbf{\Lambda}_\epsilon]_{n-k} \\ \vdots & & \ddots & \\ [\mathbf{\Lambda}_\epsilon]_{n-k}^T \tilde{\lambda}_1 & [\mathbf{\Lambda}_\epsilon]_{n-k}^T \tilde{\lambda}_2 & \dots & [\mathbf{\Lambda}_\epsilon]_{n-k}^T [\mathbf{\Lambda}_\epsilon]_{n-k} \end{pmatrix} \quad (\text{S5})$$

For the upper-left $k \times k$ block of this matrix, we have

$$\tilde{\lambda}_i^T \tilde{\lambda}_j = \tilde{\lambda}_i^T \mathbf{B}^T \mathbf{B} \tilde{\lambda}_j = (\gamma_i^*)^T \gamma_j^* = \begin{cases} 1 & \text{if } i = j \\ 0 & \text{otherwise.} \end{cases}$$

Similarly,

$$[\mathbf{\Lambda}_\epsilon]_{n-k}^T \tilde{\lambda}_j = (\mathbf{B}[\mathbf{\Lambda}_\epsilon]_{n-k})^T \gamma_j^* = \mathbf{B}_\epsilon^T \gamma_j^* = \mathbf{0},$$

by Result S2. Finally,

$$[\mathbf{\Lambda}_\epsilon]_{n-k}^T [\mathbf{\Lambda}_\epsilon]_{n-k} = (\mathbf{B}^T [\mathbf{B}_\epsilon]_{n-k})^T [\mathbf{\Lambda}_\epsilon]_{n-k} = [\mathbf{B}_\epsilon]_{n-k}^T [\mathbf{B}_\epsilon]_{n-k} = \mathbb{I}_{n-k}$$

and hence from (S5) we have $\mathbf{\Lambda}^T \mathbf{\Lambda} = \mathbb{I}_n$ as required. \square

S2.2 Gram-Schmidt invariance

Gram-Schmidt orthonormalisation is used to impose orthonormality on an arbitrary set of basis vectors $\mathbf{B} = (\mathbf{b}_1, \dots, \mathbf{b}_n)$ (Björck, 1967). The usual recursive formula can be rewritten using matrices (Björck, 1994):

$$\mathbf{B} = \mathbf{\Gamma} \mathbf{R}$$

where $\mathbf{\Gamma}$ is the $l \times n$ basis containing the normalised, orthogonal vectors $\gamma_1, \dots, \gamma_n$, and \mathbf{R} is an $n \times n$ upper-triangular matrix relating the two bases. This shows that the j^{th} new basis vector is a linear combination of the first j basis vectors of the original basis.

Result S4 (Gram-Schmidt invariance). *The reconstruction given by the first q vectors of the original basis is equal to the reconstruction given by the first q vectors of the orthogonal basis:*

$$\mathcal{R}_{\mathbf{W}}(\mathbf{B}_q, \mathbf{z}) = \mathcal{R}_{\mathbf{W}}(\mathbf{\Gamma}_q, \mathbf{z}), \quad q = 1, \dots, n$$

Proof. Using $\mathbf{\Gamma}^T \mathbf{\Gamma} = \mathbb{I}_k$ because $\mathbf{\Gamma}$ consists of orthonormal columns by construction, the reconstruction of $f(\cdot)$ with the original basis \mathbf{B} is (proceeds

similarly for any truncation \mathbf{B}_q)

$$\begin{aligned}
\mathbf{B}(\mathbf{B}^T \mathbf{B})^{-1} \mathbf{B}^T \mathbf{z} &= \mathbf{\Gamma} \mathbf{R} ((\mathbf{\Gamma} \mathbf{R})^T \mathbf{\Gamma} \mathbf{R})^{-1} (\mathbf{\Gamma} \mathbf{R})^T \mathbf{z} \\
&= \mathbf{\Gamma} \mathbf{R} (\mathbf{R}^T \mathbf{\Gamma}^T \mathbf{\Gamma} \mathbf{R})^{-1} \mathbf{R}^T \mathbf{\Gamma}^T \mathbf{z} \\
&= \mathbf{\Gamma} \mathbf{R} (\mathbf{R}^T \mathbf{R})^{-1} \mathbf{R}^T \mathbf{\Gamma}^T \mathbf{z}
\end{aligned}$$

Then, using that \mathbf{R} is invertible and the identity $(\mathbf{C}\mathbf{D})^{-1} = \mathbf{D}^{-1}\mathbf{C}^{-1}$ for square matrices \mathbf{C} and \mathbf{D} ,

$$\begin{aligned}
&= \mathbf{\Gamma} \mathbf{R} \mathbf{R}^{-1} \mathbf{R}^{-T} \mathbf{R}^T \mathbf{\Gamma}^T \mathbf{z} \\
&= \mathbf{\Gamma} \mathbf{\Gamma}^T \mathbf{z} \tag{S6} \\
&= \mathbf{\Gamma} (\mathbf{\Gamma}^T \mathbf{\Gamma})^{-1} \mathbf{\Gamma}^T \mathbf{z}
\end{aligned}$$

i.e. the reconstruction using the new basis $\mathbf{\Gamma}$. □

Kuttler (2012) proves this result by showing that both bases span the same q -dimensional subspace, and using that a basis allows general fields to be written as a unique linear combination of the basis vectors.

S3 CanAM4

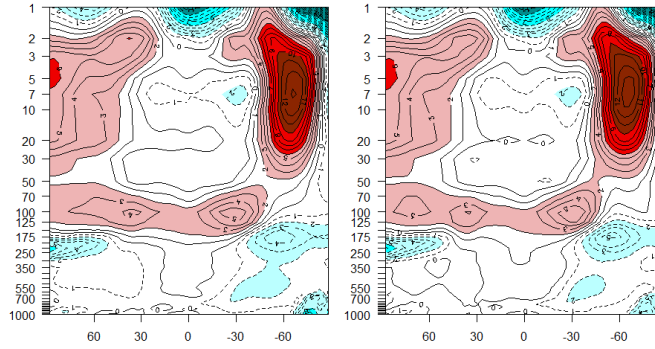


Figure S9: The TA anomaly for the standard run (left), and for run 005 of the new ensemble, the run that minimises the root mean squared error for TA in the wave 2 ensemble. There remains a large warm bias in the Southern Hemisphere, with a largely unchanged magnitude.

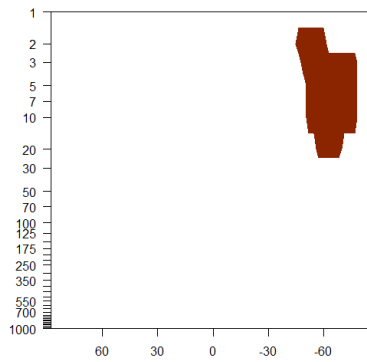


Figure S10: The grid boxes where the discrepancy is increased for TA, as described in Section 5.